# Wall modes

Edgar Knobloch

Department of Physics
University of California, Berkeley, CA 94720, USA

IPAM, 29 January 2025

with Benjamin Favier (IRPHE) and many others

"Rotating Convection: From the Lab to the Stars" workshop held at the Lorentz Center in Leiden, Netherlands, May 28 - June 1, 2018, organized by R. Ecke, K. Julien, P. Garaud, S. Weiss and R. Kunnen

# A bit of history

*J. Fluid Mech.* (1969), *vol.* 36, *part* 2, *pp.* 309–335
*Printed in Great Britain*



## A study of Bénard convection with and without rotation

By H. T. ROSSBY†
Department of Meteorology
Massachusetts Institute of Technology

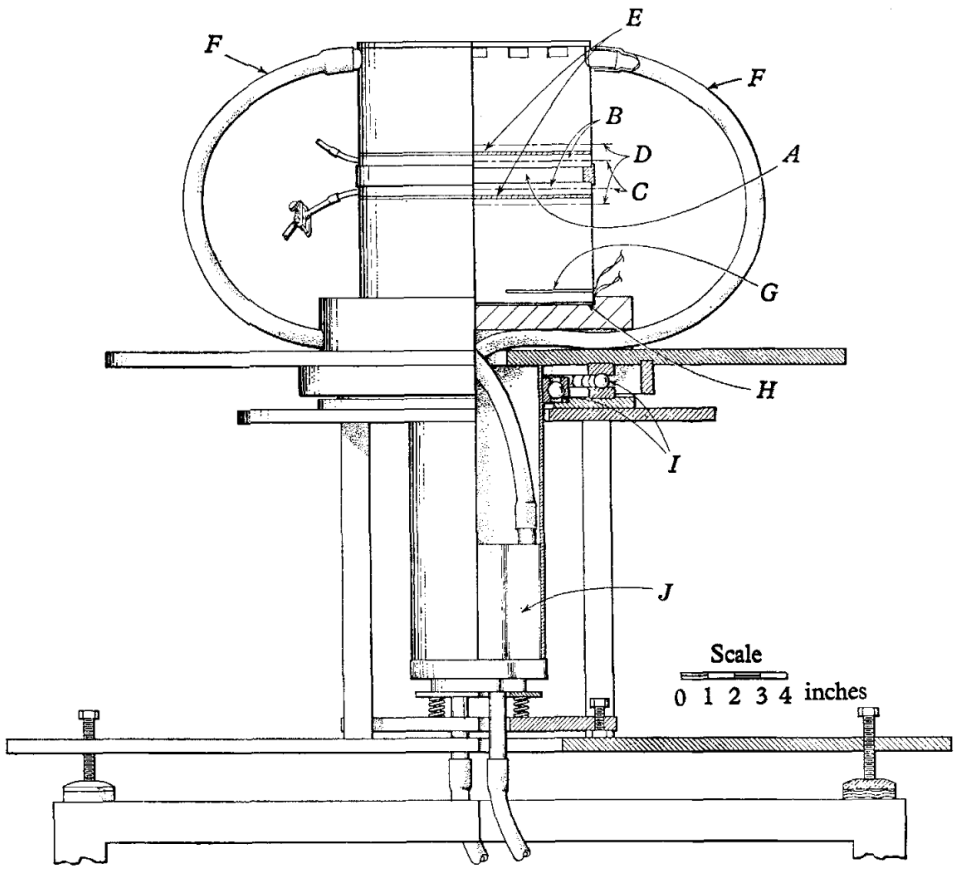

# A bit of history

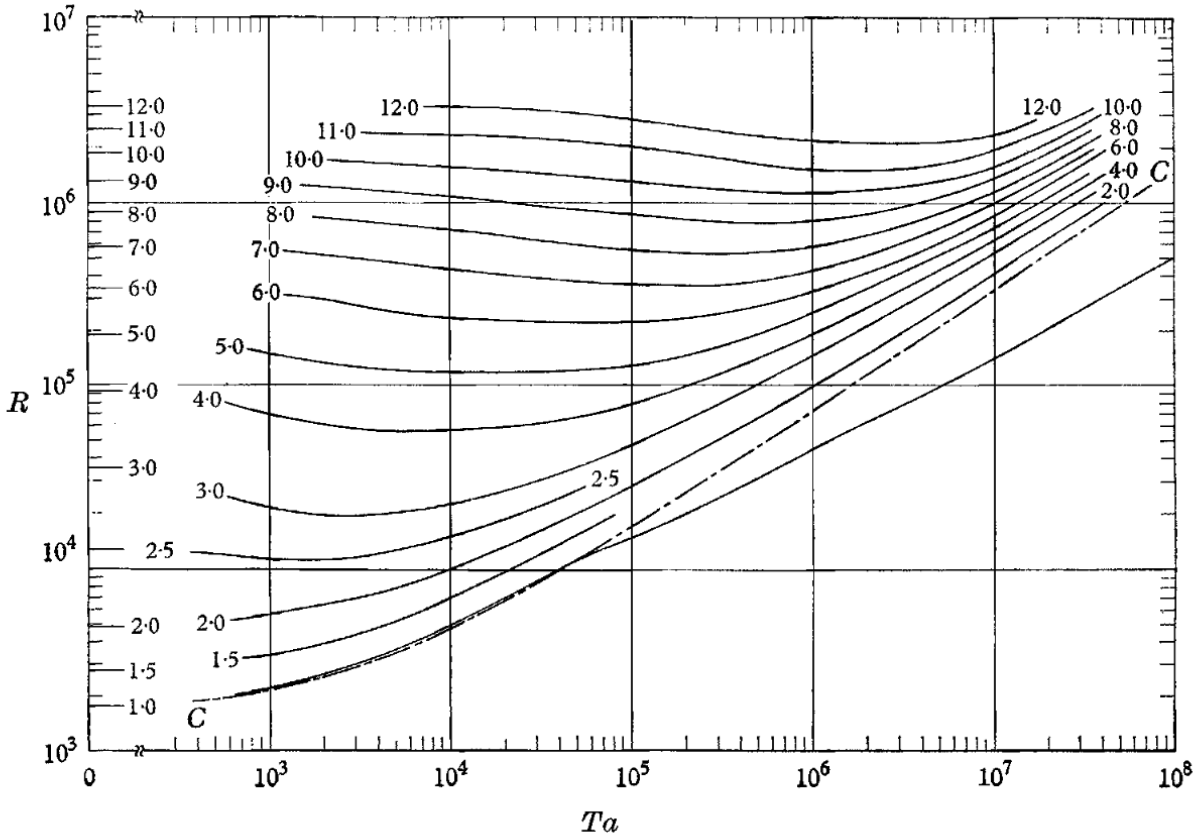


FIGURE 11. Lines of constant Nusselt number as a function of the Rayleigh and Taylor numbers in water with Prandtl number 6·8. Except for small values of the Nusselt number at large Taylor numbers the error in the Nusselt number is $\lesssim \pm 2\,\%$.

*Water*

The dot-dashed line $C$–$C$ in figure 11 is the marginal stability curve according to Chandrasekhar (1961). We find excellent agreement between theory and experiment for the critical Rayleigh number at all Taylor numbers less than $5 \times 10^4$; beyond this the fluid becomes unstable at lower Rayleigh numbers

# A bit of history

J.C. Buell and I. Catton, Effect of rotation on the stability of a bounded cylindrical layer of fluid heated from below, Phys. Fluids **26**, 892 (1983):

**TABLE I.** Critical Rayleigh numbers $R_c \times 10^{-3}$ (and corresponding mode numbers $n$) as a function of Taylor number ($D = \mathrm{Ta}^{1/2}$) and aspect ratio ($A$) for conducting walls.[a]

| $D$ \ $A$ | 0.2 | 0.25 | 0.35 | 0.5 | 0.7 | 1.0 | 1.5 | 2.0 | $\infty$ [b] |
|---|---|---|---|---|---|---|---|---|---|
| 0.0 | 151.2(1) | 66.6(1) | 21.3(1) | 8.01(1) | 4.35(1) | 2.54(0) | 2.01(0) | 1.88(1) | 1.71 |
| 50 | 151.2(1) | 66.6(1) | 21.4(1) | 8.20(1) | 4.71(1) | 3.46(0) | 3.04(1) | 2.91(2) | 2.71 |
| 100 | 151.3(1) | 66.8(1) | 21.7(1) | 8.77(1) | 5.76(1) | 5.09(2) | 4.85(4) | 4.90(3) | 4.71 |
| 200 | 151.7(1) | 67.4(1) | 22.8(1) | 10.9 (1) | 9.51(1) | 9.22(3) | 9.48(4) | 9.59(4) | 9.80 |
| 400 | 153.2(1) | 69.7(1) | 27.2(1) | 18.6 (1) | 18.8 (2) | 19.5 (3) | 19.5 (4) | 19.9 (4) | 22.2 |
| 600 | 155.7(1) | 73.5(1) | 33.9(1) | 29.5 (1) | 30.5 (2) | 30.6 (3) | 30.8 (4) | 31.3 (4) | 36.7 |
| 800 | 159.2(1) | 78.7(1) | 42.8(1) | 42.5 (1) | 43.0 (2) | 42.6 (3) | 43.0 (4) | 43.7 (4) | 53.1 |
| 1000 | 163.5(1) | 85.2(1) | 53.5(1) | 55.3 (2) | 55.6 (2) | 55.5 (3) | 56.1 (4) | 57.0 (4) | 71.1 |
| 1200 | 168.8(1) | 92.9(1) | 65.9(1) | 69.2 (2) | 68.8 (2) | 69.2 (3) | 69.9 (4) | 71.0 (4) | 90.7 |
| 1400 | 174.9(1) | 101.7(1) | 79.8(1) | 83.7 (1) | 82.9 (2) | 83.4 (3) | 84.4 (4) | 85.7 (4) | 111.7 |

[a] Only $n<4$ is considered here; higher $n$ may be slightly more unstable for the higher aspect ratios.
[b] The last column(s) list Chandrasekhar's results (Ref. 1).

Here $A = R/H$ is the aspect ratio, while $D = Ta^{1/2}$ is the inverse Ekman number.

J.C. Buell and I. Catton, The effect of wall conduction on the stability of a fluid in a right circular cylinder heated from below, J. Heat Transfer **105**, 255 (1983), examined the effect of different radial boundary conditions in the nonrotating case.

# Cylindrical domain: wall modes precess

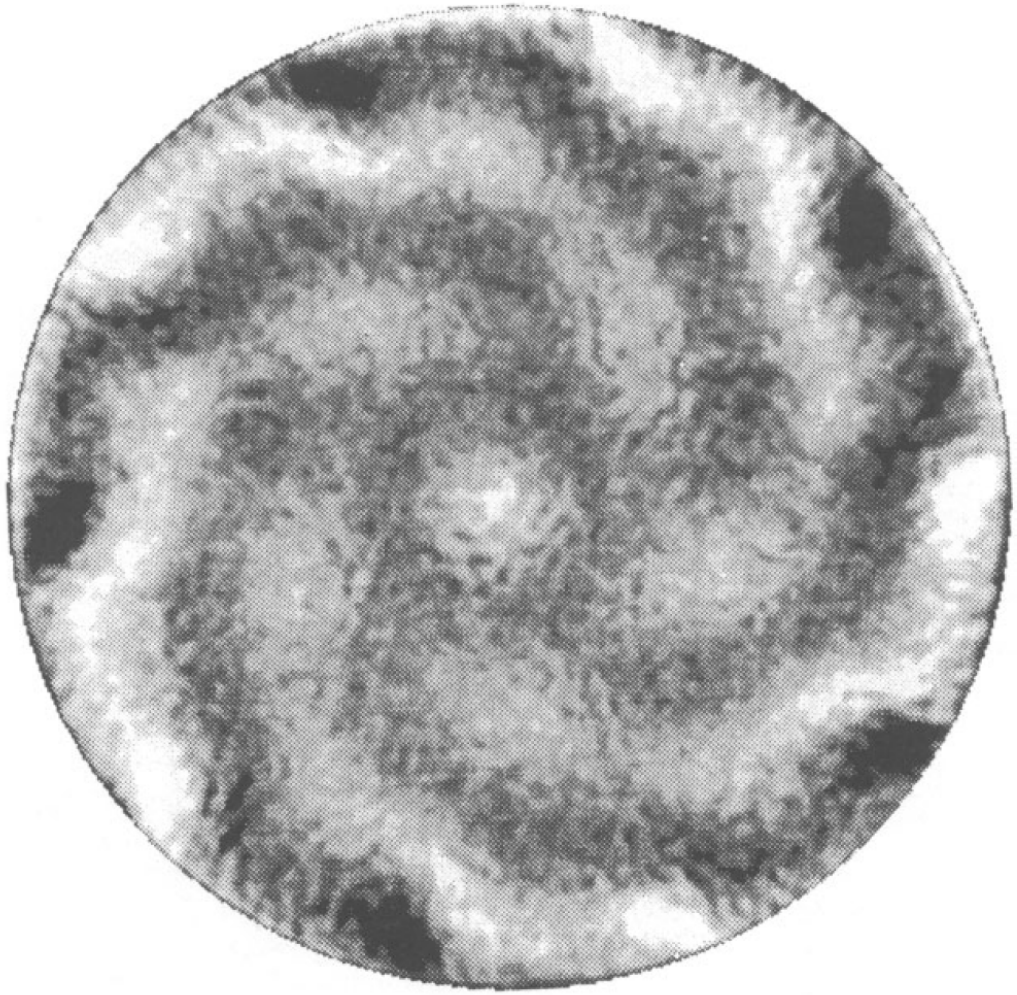

Fig. 4. – Shadowgraph image of the $m = 5$ state for $\Omega = 2145$ and $\varepsilon = 2.6$. The entire pattern precesses in the rotating frame at constant velocity.

Zhong et al., PRL**67** 2473 (1991); Ecke et al., EPL **19**, 177 (1992).

# Linear theory: wall modes precess



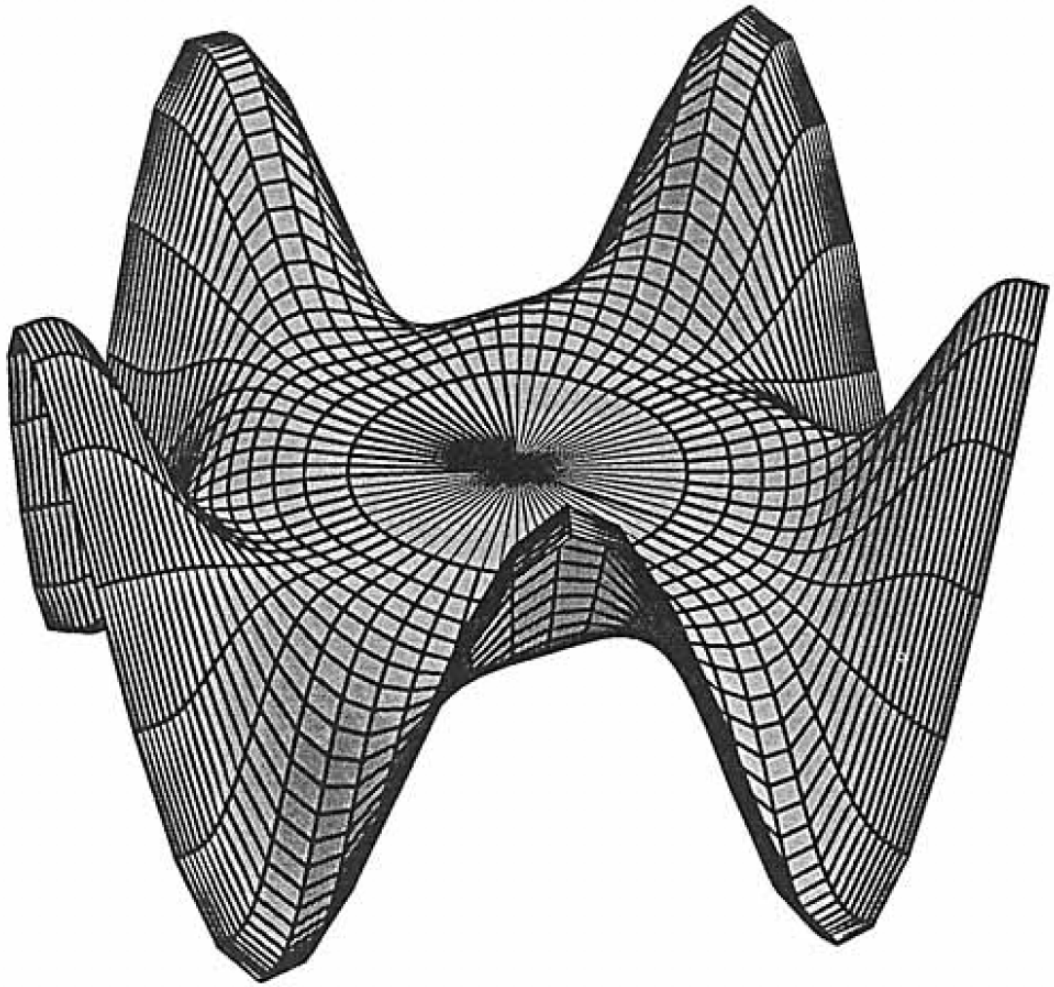

FIGURE 2. A plot of $\Theta$ $(z = \frac{1}{2})$ for an $m = 5$ fast mode at $\Omega = 500$, $\sigma = 7.0$ in a $\Gamma = 1$ cylinder, for boundary conditions A. For this mode $R_c^{(5)} = 35989.6$, $\omega_c^{(5)} = 26.884$.

Goldstein et al., JFM **248**, 583 (1993)

# Linear theory: wall modes precess



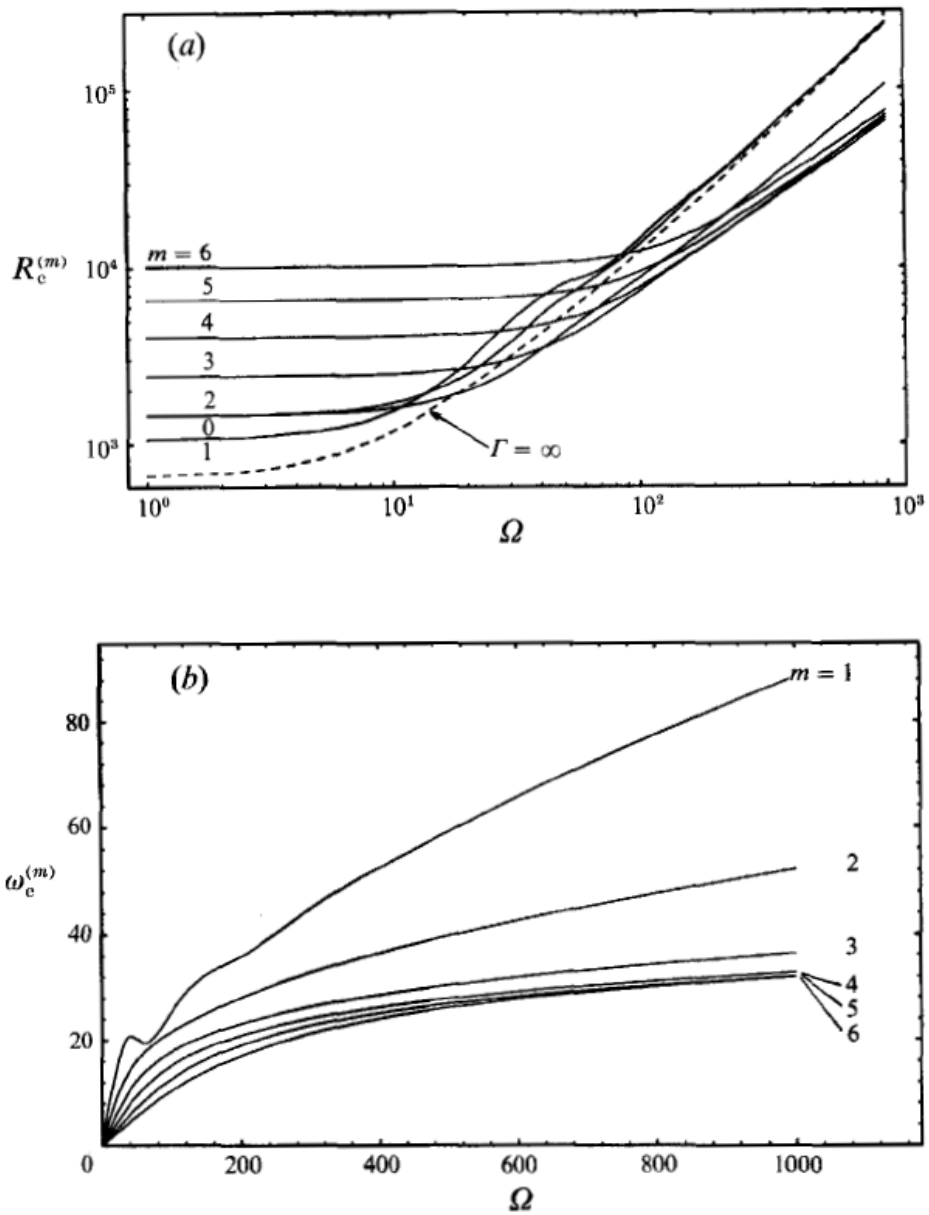

# Linear theory: bulk modes also precess

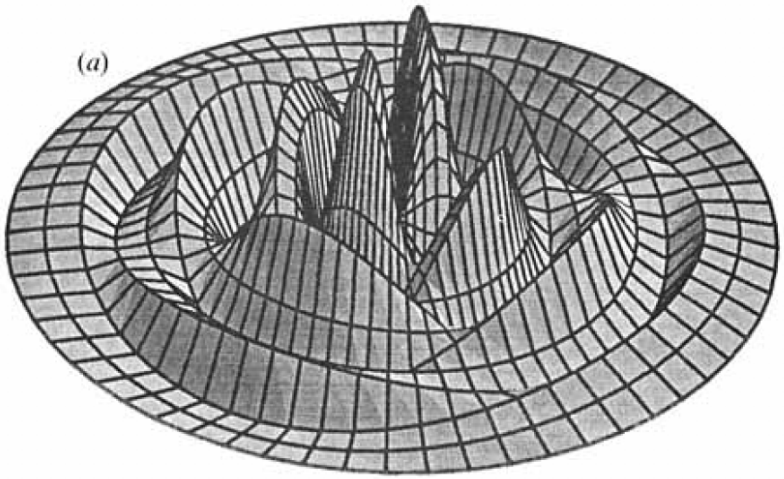


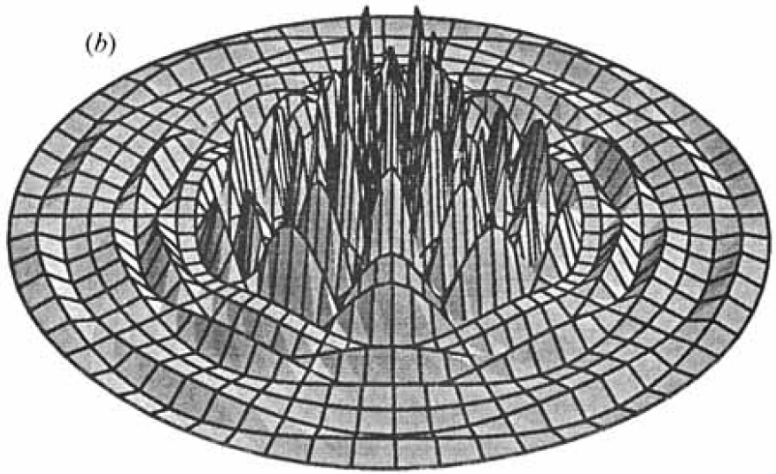


$m = 2$, $\Gamma = 1.84$ $m = 5$, $\Gamma = 4.39$

The wall and bulk modes display very different behavior with respect to the domain aspect ratio $\Gamma$:

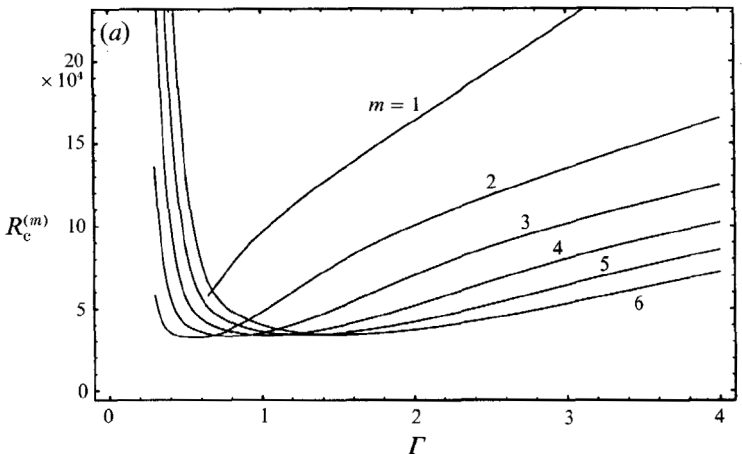


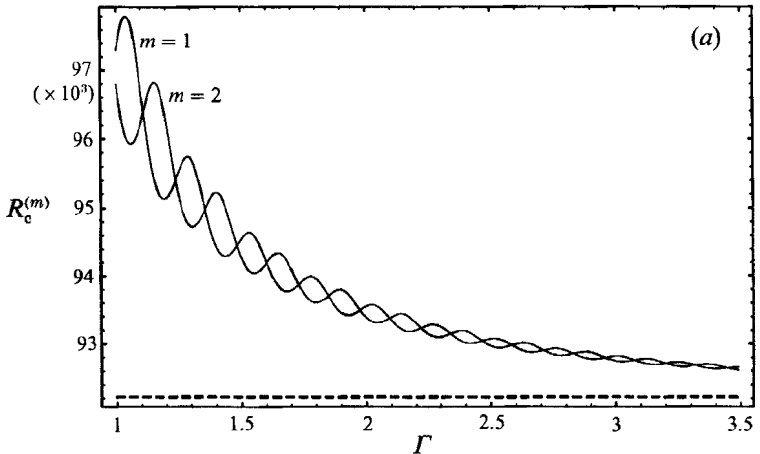

# Wall modes in a cylinder: theory

To understand the properties of wall modes we employ polar coordinates $(r, \phi, z)$ and suppose that the wall mode has azimuthal wavenumber $m > 0$, i.e. that the mode breaks the azimuthal invariance of the system. Near onset we may write the temperature departure from the conduction state in the form

$$\theta(r, \phi, z, t) = \mathcal{R}\{a_m(t) \exp(-im\phi) f_m(r, z)\} + \dots,$$

where $f_m(r, z)$ is the eigenfunction of the mode $m$ and $a_m$ is its amplitude. When the cylinder does not rotate and the boundary conditions are $\phi$-independent, the equation satisfied by $a_m$ must commute with the symmetries

$$\begin{aligned} &\text{rotations}: && \phi \to \phi + \phi_0: && a_m \to a_m \exp(-im\phi_0), \\ &\text{reflection}: && \phi \to -\phi: && a_m \to \bar{a}_m. \end{aligned}$$

It follows that $\dot{a}_m = g(|a_m|^2, \varepsilon) a_m$, where $g$ is necessarily real. The parameter $\varepsilon \equiv (\mathrm{Ra} - \mathrm{Ra}_w)/\mathrm{Ra}_w$ measures the distance from onset; $\mathrm{Ra}_w$ also depends on the mode number $m$.

# Wall modes in a cylinder: theory

Near onset $\varepsilon \ll 1$ and the function $g$ may be expanded in a Taylor series:

$$\dot{a}_m = \varepsilon a_m + \alpha |a_m|^2 a_m + \dots$$

Writing $a_m = A_m \exp(i\Phi_m)$ we see that the onset of a steady-state instability is described by equations of the form

$$\dot{A}_m = \varepsilon A_m + \alpha A_m^3 + \dots, \qquad \dot{\Phi}_m = 0.$$

The latter is a consequence of neutral stability of the mode with respect to rotations and shows that the bifurcation is a pitchfork of revolution.
Now suppose that the cylinder rotates with a small angular velocity $\Omega$. The rotation breaks the reflection symmetry but not the rotation symmetry. The coefficients consequently acquire nonzero imaginary parts:

$$\dot{a}_m = (\varepsilon + i\Omega\delta) a_m + (\alpha + i\Omega\beta) |a_m|^2 a_m + \dots,$$

where $\varepsilon$, $\delta$, $\alpha$ and $\beta$ are all functions of $\Omega^2$ and the mode number $m$.

# Wall modes in a cylinder: theory

In terms of the real variables we now have

$$\dot{A}_m = \varepsilon A_m + \alpha A_m^3 + \dots, \qquad \dot{\Phi}_m = \Omega(\delta + \beta A_m^2 + \dots)$$

and conclude that the bifurcation leads to a precessing state of the form

$$\theta = \mathcal{R}\{A_m \exp[i(\omega_d t - m\phi)]\, f_m(r,z)\} + \dots$$

with drift frequency

$$\omega_d = \Omega\left(\delta - \frac{\beta}{\alpha}\varepsilon\right) + \mathcal{O}(\varepsilon^2).$$

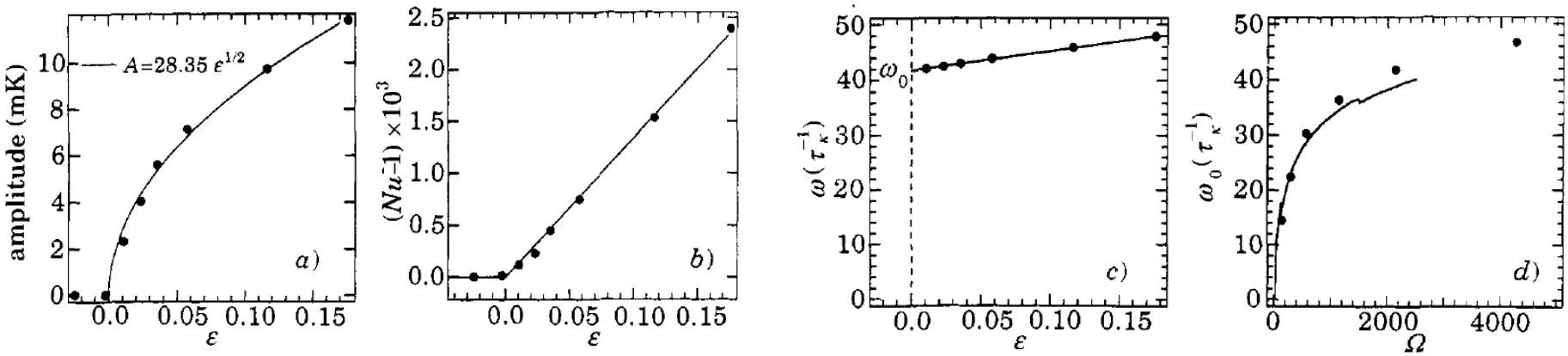


Ecke et al. Europhys. Lett. **19**, 177-182 (1992).

# Cylindrical domain: $\sigma < 0.68$, $E = 10^{-3}$, $\Gamma = 2$

For stress-free top and bottom: $m = 0$ mode

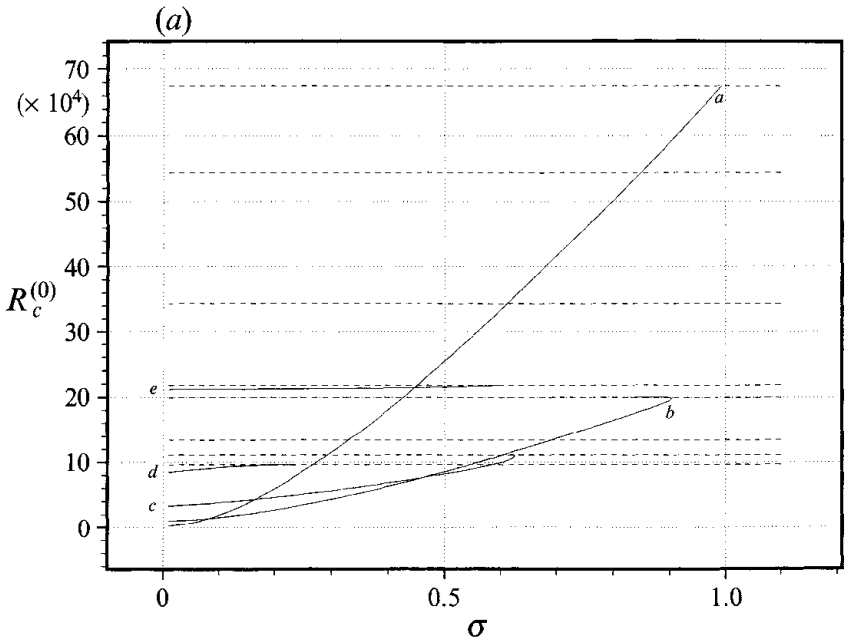


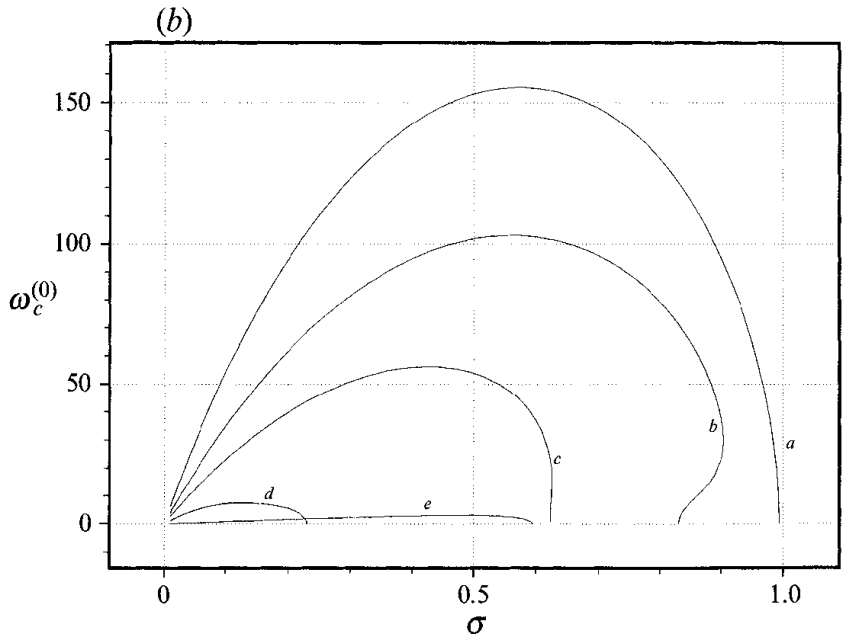


Goldstein et al., JFM **262**, 293-324 (1994)

# Cylindrical domain: $\sigma < 0.68$, $E = 10^{-3}$, $\Gamma = 2$

For stress-free top and bottom: $m = 1$ mode

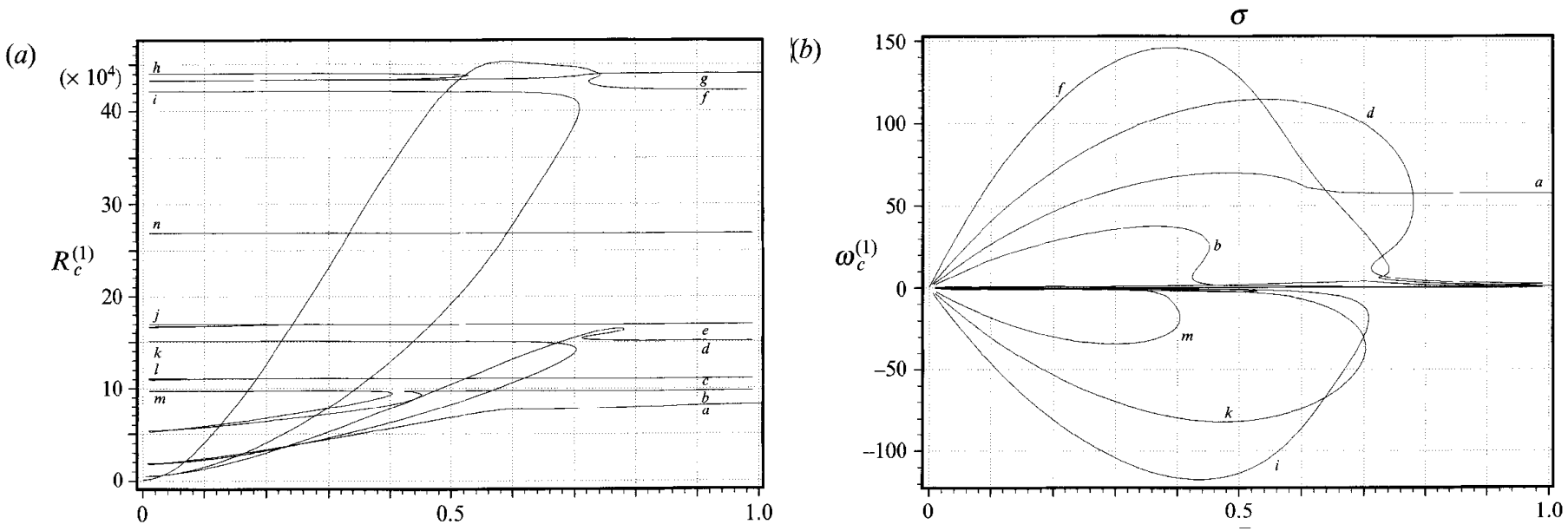


Goldstein et al., JFM **262**, 293-324 (1994)

# Cylindrical domain: wall modes for $\sigma < 0.68$, $m \neq 0$



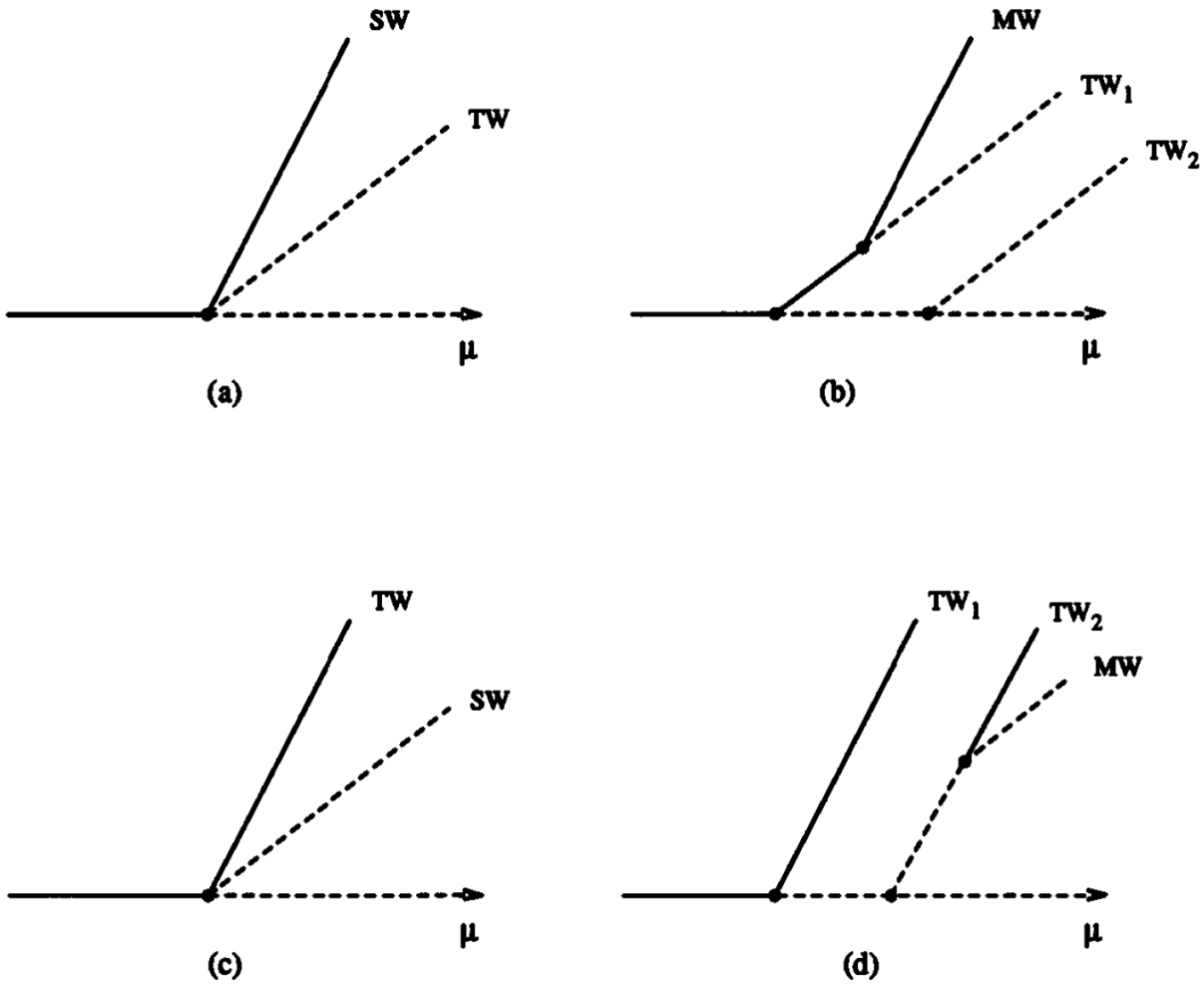


Bifurcations in rotating systems, in Lectures on Solar and Planetary Dynamos (M.R.E. Proctor and A.D. Gilbert, eds), pp 331-372 (1994)

# A bit more history: $\sigma \gtrsim 0.68$, insulating wall

J. Herrmann and F.H. Busse, Asymptotic theory of wall-attached convection in a rotating fluid layer, JFM **255**, 183 (1993):

$$Ra_{bulk} \approx 3(\pi^2/2)^{2/3} E^{-4/3}, \qquad Ra_{wall} \approx \pi^2 (6\sqrt{3})^{1/2} E^{-1}$$

as $E \to 0$, while $\omega_{wall} \approx -59E/\sigma$ is the asymptotic precession frequency.

M.C. Cross and E. Kuo, Traveling-wave wall states in rotating Rayleigh-Bénard convection, PRE **47**, R2245 (1993):

$$\tau_0 \left( \frac{\partial A}{\partial t} + s \frac{\partial A}{\partial x} \right) = \epsilon(1 + ic_0)A + \xi_0^2 (1 + ic_1) \frac{\partial^2 A}{\partial x^2} - g(1 + ic_3)|A|^2 A$$

and calculated the coefficients for a planar wall of finite conductivity:

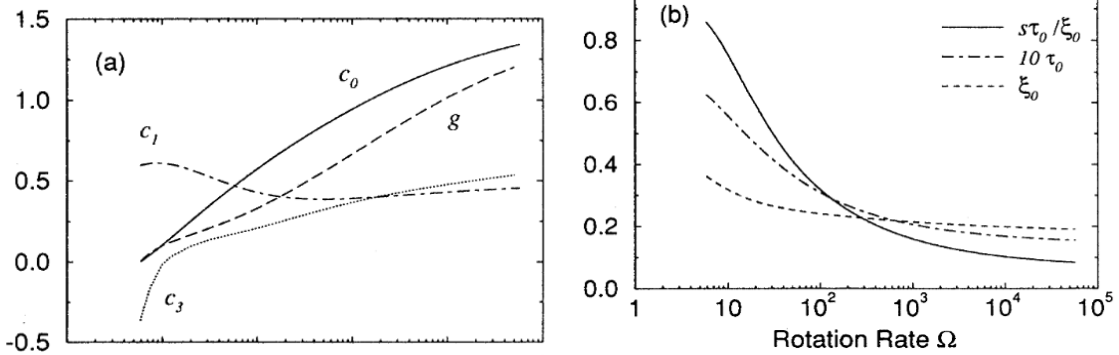

# Cylindrical domain: wall modes vs bulk modes

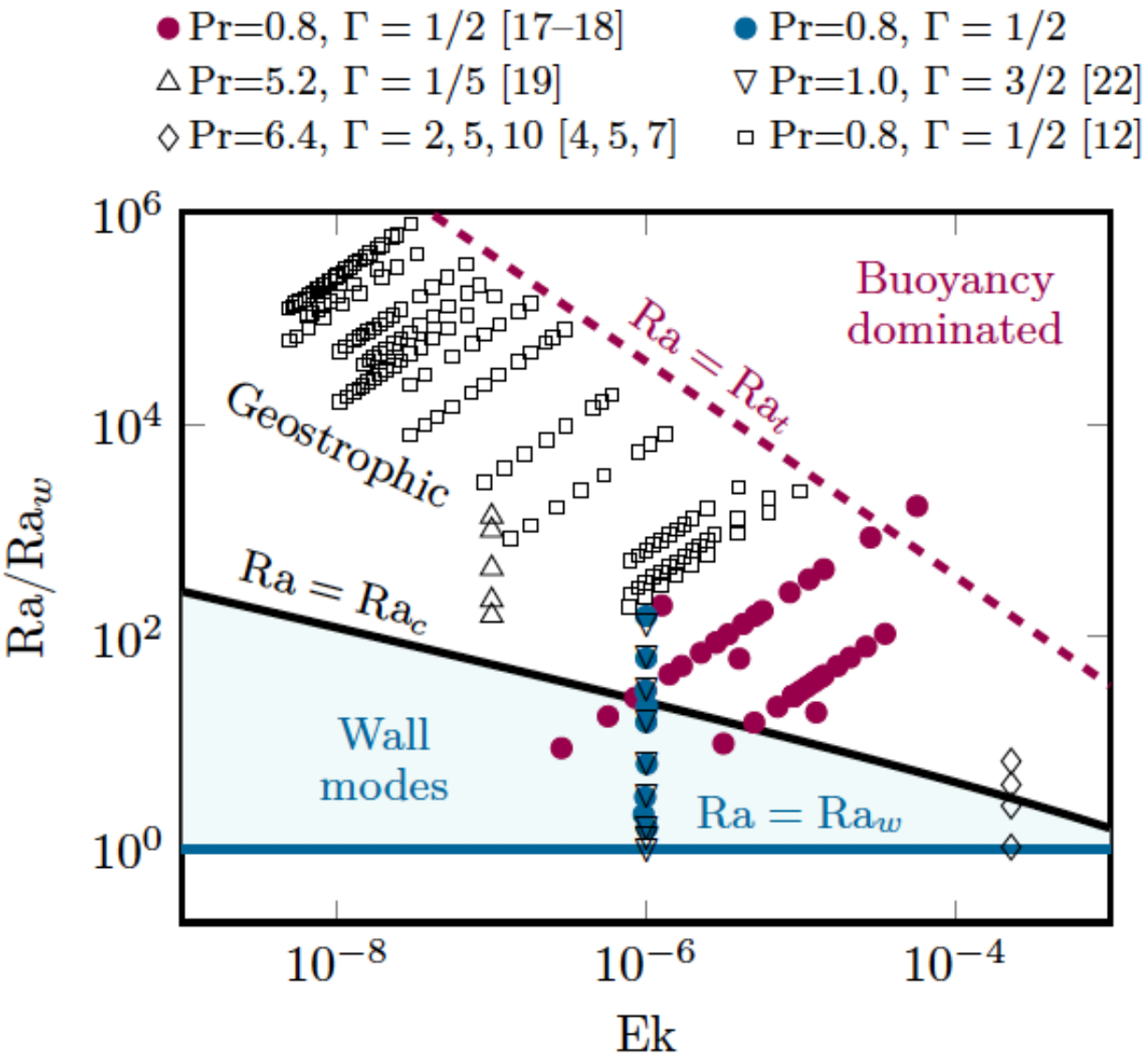


Ecke et al., PR Fluids **7**, L011501 (2022); cf. Goldstein et al., JFM **248**, 583 (1993), Zhang et al., JFM **915**, A62 (2021)

# Boundary zonal flow and walls modes: $\Gamma = 0.2$

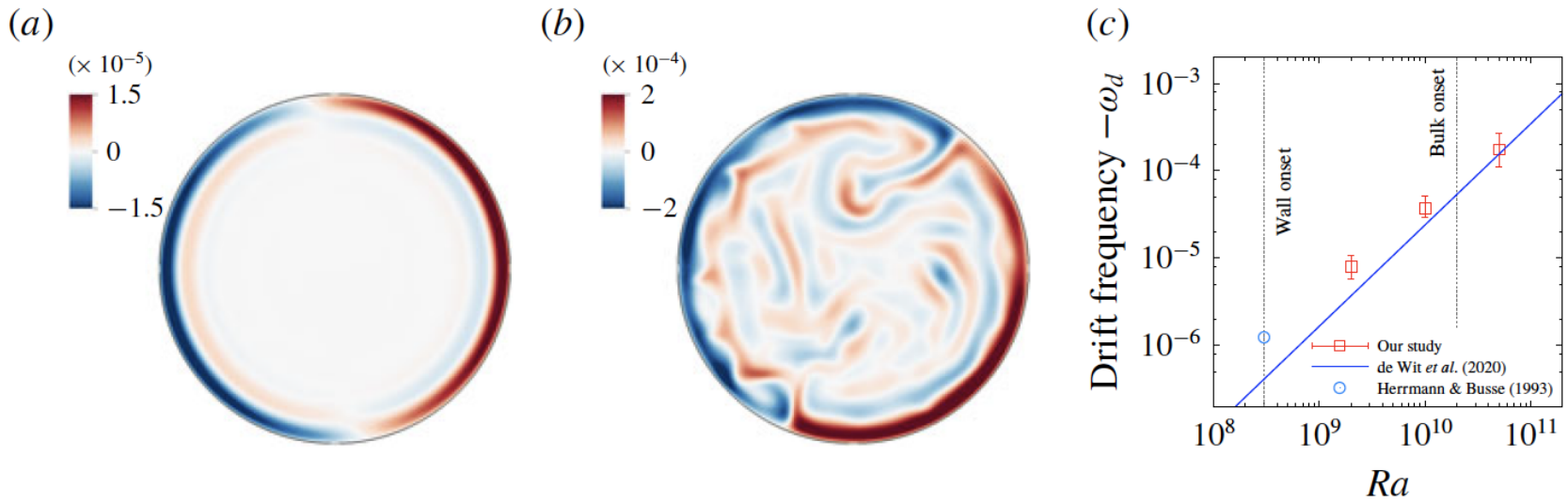


FIGURE 5. Vertical velocity in the mid-plane $z = 0.5$ in a $\Gamma = 0.2$ cylinder rotating at $E = 10^{-7}$ with $Pr = 5.2$ and (*a*) $Ra = 2 \times 10^9$ and (*b*) $Ra = 5 \times 10^{10}$ (this latter case can be compared with figure 2*b* of de Wit *et al.* (2020) at exactly the same parameters). (*c*) Drift frequency $-\omega_d$ as a function of $Ra$. The theoretical value $\omega_d = \omega_c \approx -63E/Pr$ predicted by Herrmann & Busse (1993) for the onset of the instability in the presence of a planar wall is also reported (open circle). The oblique line corresponds to the scaling $\omega_d \approx -6 \times 10^{-10} Ra^{1.16} E$ reported in de Wit *et al.* (2020) and obtained at much larger $Ra$.

Favier and Knobloch, JFM **895**, R1 (2020)
Zhang et al., JFM **915**, A62 (2021)

# Wall modes: $E = 10^{-6}$, $\sigma = 1$, $\Gamma = 1.5$

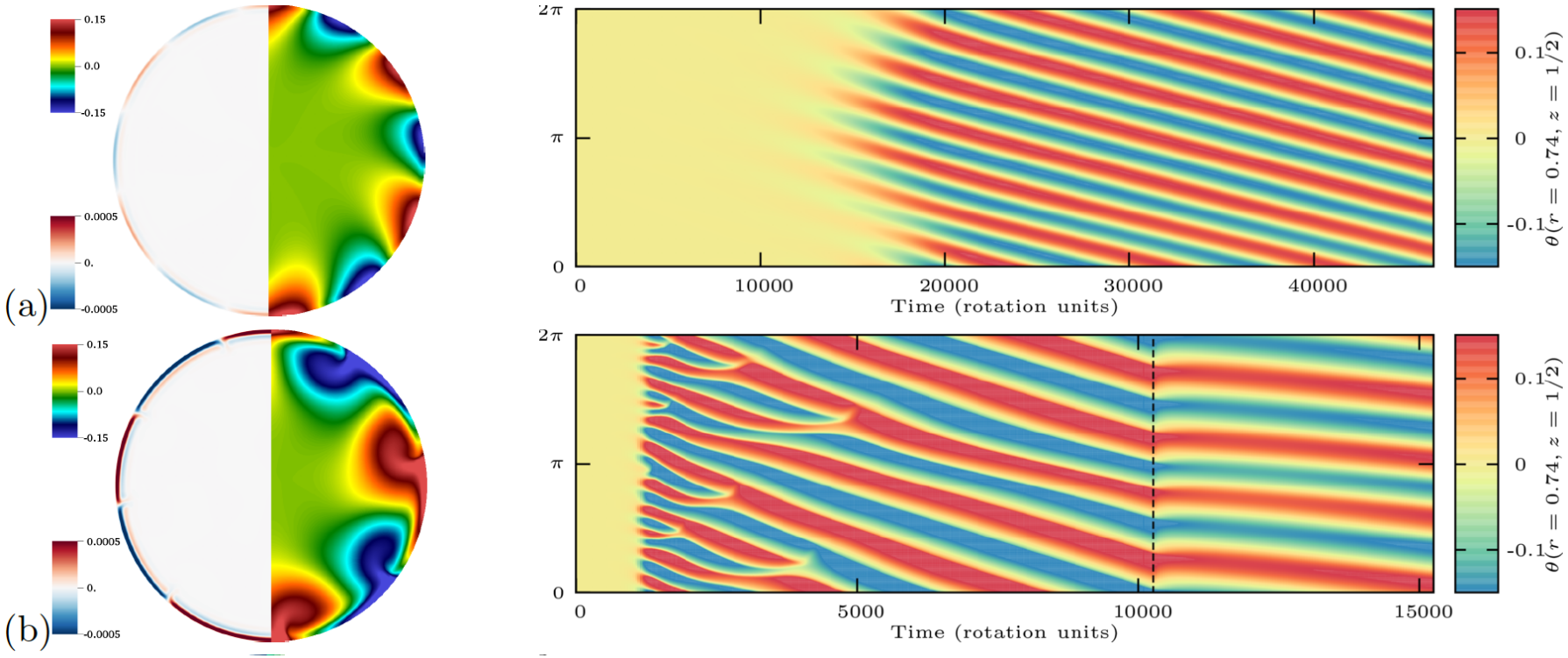


Midplane vertical velocity $w$ (left) and fluctuating temperature $\theta$ at $r = 0.74$ (right) at (a) $Ra = 5 \times 10^7$ and (b) $Ra = 2 \times 10^8$. In (b) $Ra$ is reduced to $Ra = 5 \times 10^7$ at the dashed line to demonstrate multistability.

Favier and Knobloch, JFM **895**, R1 (2020)

# Robust wall flow: $E = 10^{-6}$, $\sigma = 1$, $\Gamma = 1.5$

Wall states persist in the presence of a turbulent bulk state in the interior:

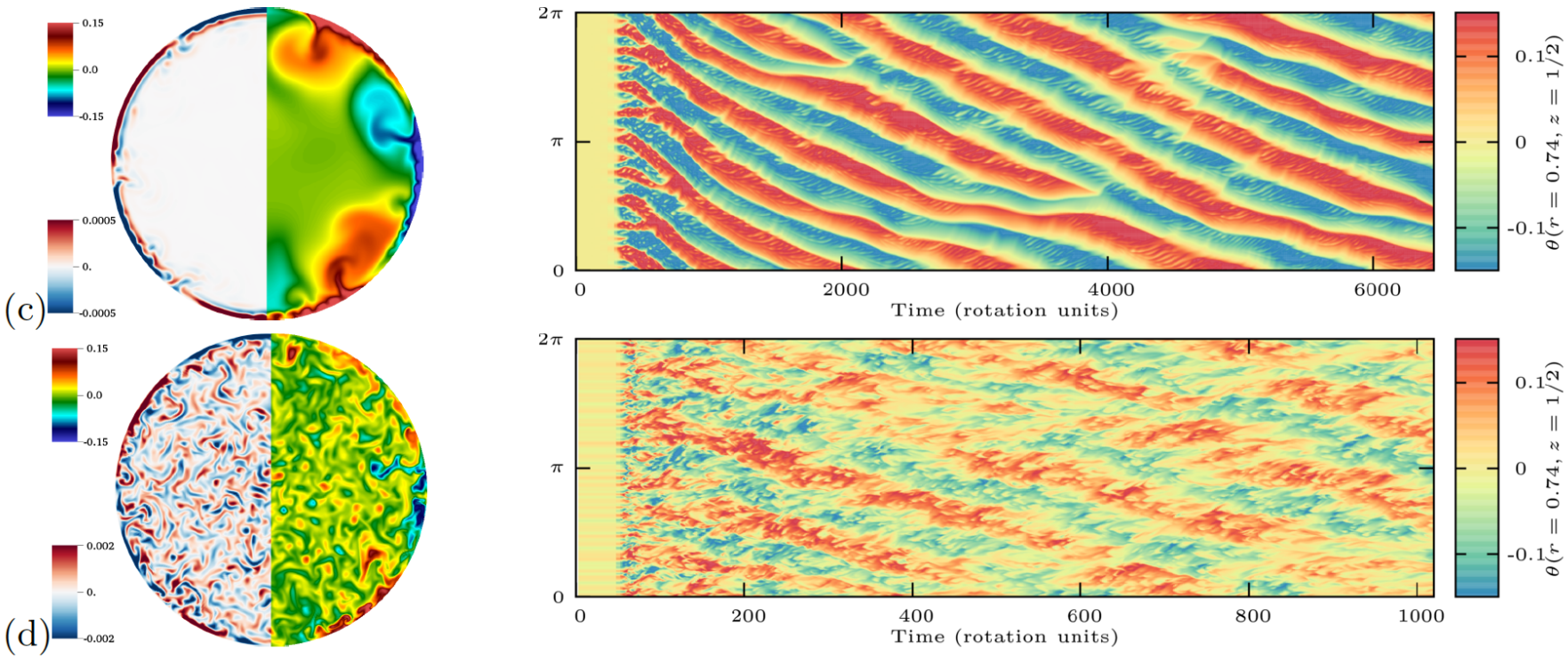


Midplane vertical velocity $w$ (left) and fluctuating temperature $\theta$ (right) at (c) $Ra = 5 \times 10^8$ and (d) $Ra = 2 \times 10^9$.

Favier and Knobloch, JFM **895**, R1 (2020); Zhang et al., JFM **915**, A62 (2021)

# Robust wall flow: $E = 10^{-6}$, $\sigma = 1$, $\Gamma = 1.5$

Wall states persist in the presence of a vertical barrier:

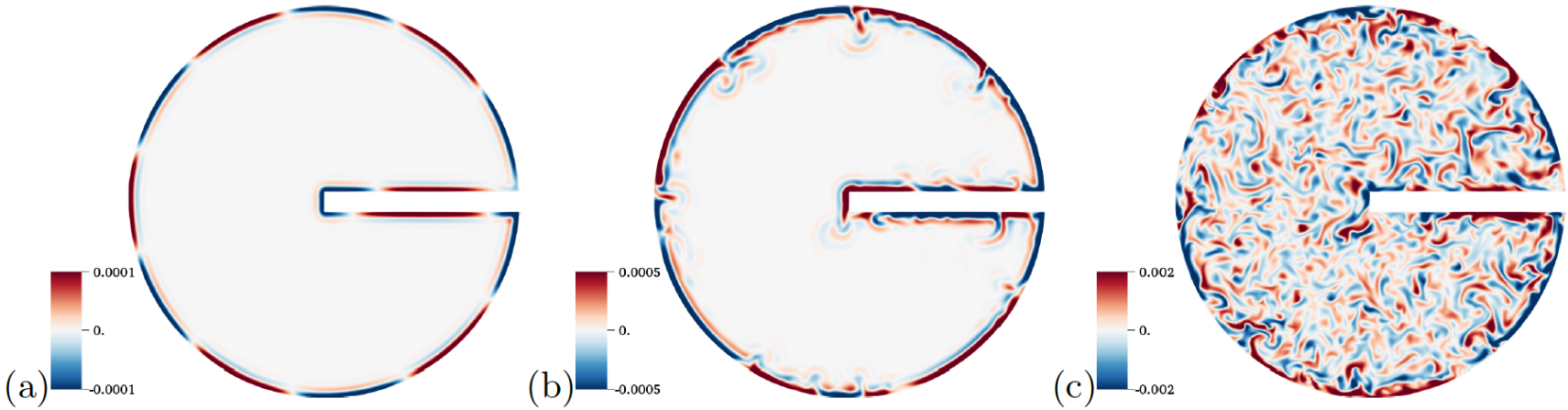


FIGURE 5. Vertical velocity in the mid-plane $z = 0.5$ for a cylinder with a barrier. The Rayleigh number increases from left to right: (a) $Ra = 5 \times 10^7$, (b) $Ra = 5 \times 10^8$ and (c) $Ra = 2 \times 10^9$. Parameters are $\Gamma = 1.5$, $E = 10^{-6}$ and $Pr = 1$.

Favier and Knobloch, JFM **895**, R1 (2020)

# Robust wall flow: $E = 10^{-6}$, $\sigma = 1$, $\Gamma = 1.5$

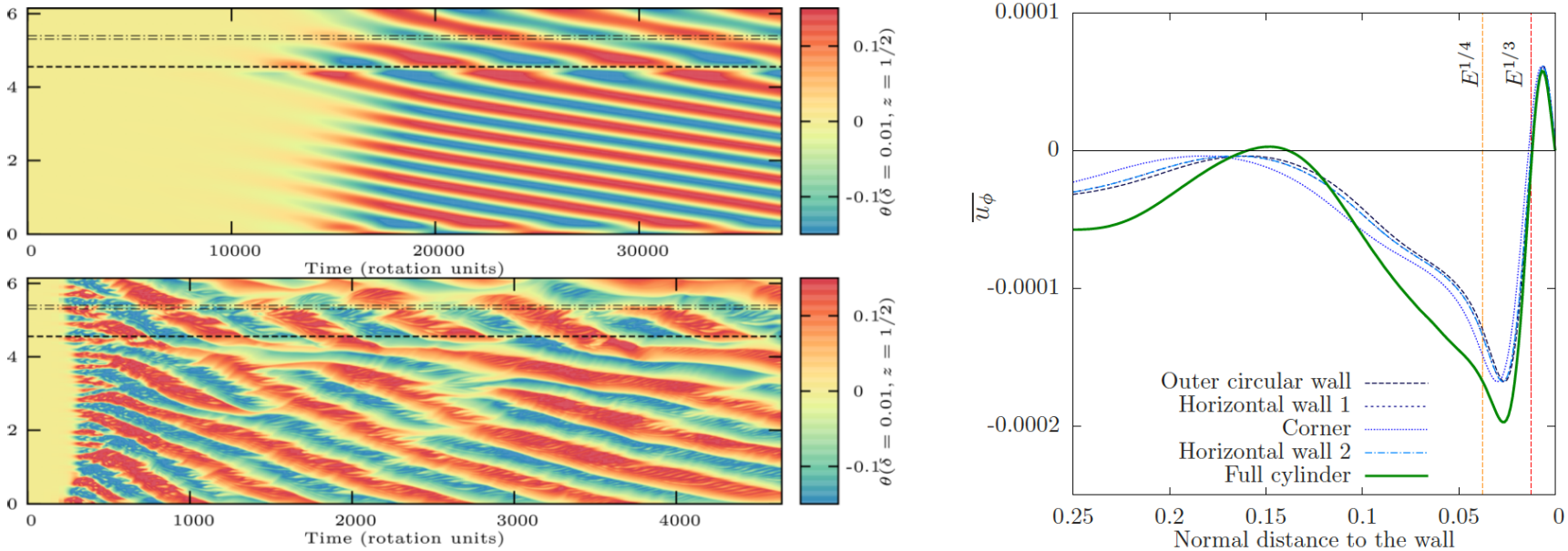


FIGURE 6. Left: spatio-temporal plots showing the temperature fluctuation $\theta$ at $z = 0.5$ and a fixed distance $\delta = 10^{-2}$ from the boundary at $Ra = 5\times10^7$ (top panel) and $Ra = 5\times10^8$ (bottom panel). The vertical axis represents the arclength along the boundary while the horizontal axis is time (in rotation units). The dotted lines indicate the positions of the four corners of the barrier. Parameters are $\Gamma = 1.5$, $E = 10^{-6}$ and $Pr = 1$. Right: vertical and temporal average of the velocity component tangential to the boundary at $Ra = 5 \times 10^8$. We distinguish between the cylindrical boundary and the different faces of the barrier. The results are compared to the case without barrier (see figure 3(b)).

Favier and Knobloch, JFM **895**, R1 (2020)

# Robust wall flow: $E = 10^{-6}$, $\sigma = 1$, $\Gamma = 1.5$

Precession frequency with and without barrier:

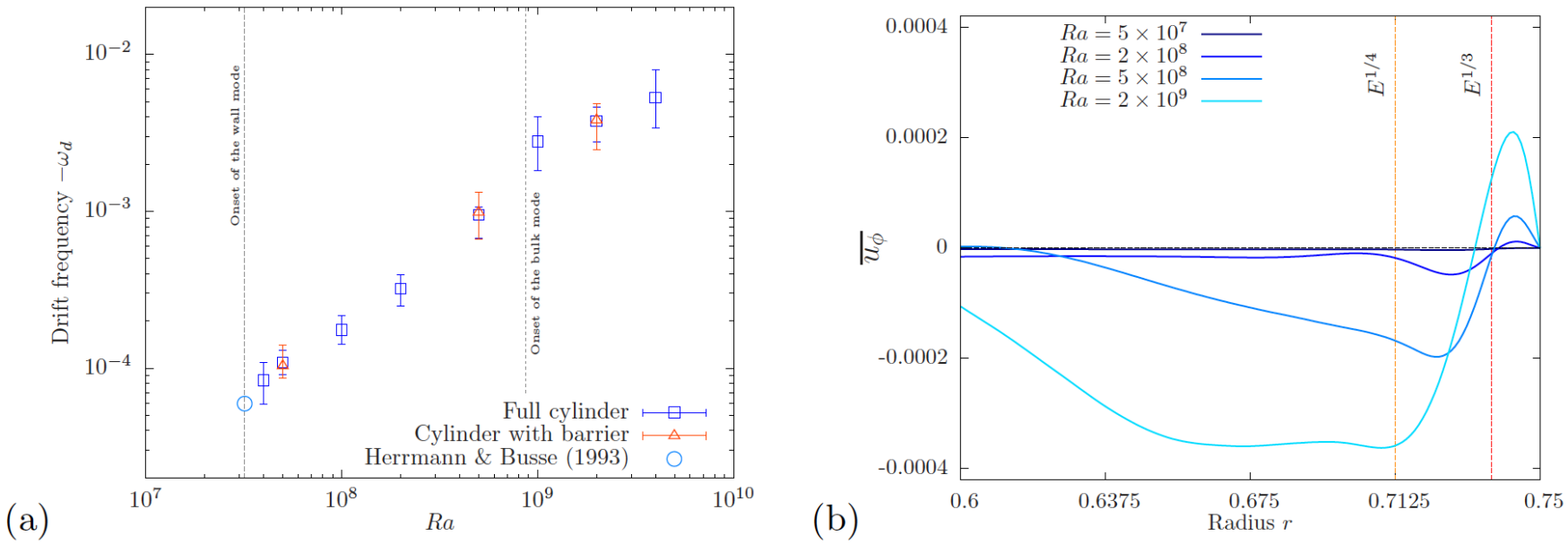


FIGURE 3. Left: drift frequency $\omega_d$ as a function of $Ra$ for $\Gamma = 1.5$, $E = 10^{-6}$ and $Pr = 1$. The results for the full cylinder (□) and the cylinder with a barrier (△, see section 5 below) coincide. The theoretical value $\omega_d = \omega_c \approx -59E/Pr$ predicted by Herrmann & Busse (1993) for the onset of the instability in the presence of a planar wall is also reported (open circle). Right: azimuthally, vertically and temporally averaged zonal velocity as a function of the radial coordinate $r$. Positive values correspond to cyclonic motions while negative values correspond to anti-cyclonic motions. The two vertical lines indicate the Stewartson layer scales $E^{1/3}$ and $E^{1/4}$ (Stewartson 1957).

Favier and Knobloch, JFM **895**, R1 (2020)

# Sound waves in chiral systems with odd viscosity

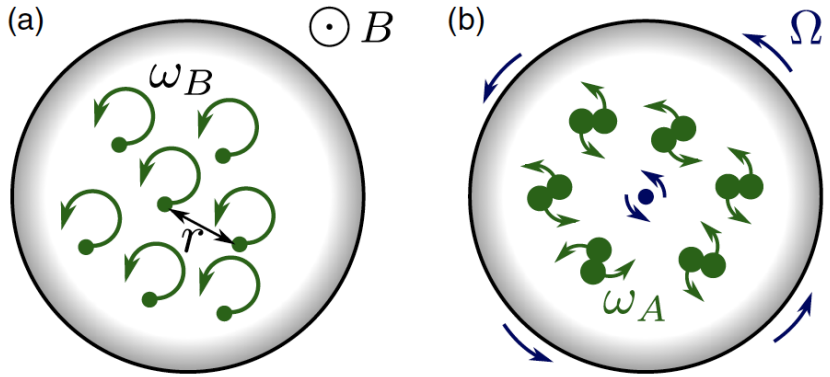


FIG. 1. Physical realizations of the minimal model for topological fluids with odd viscosity. (a) Two-dimensional plasma under magnetic field $B$, with cyclotron frequency $\omega_B = qB/M$. (b) Chiral active fluid with intrinsic rotation angular frequency $\omega_A$, subject to a global rotation with angular frequency $\omega_B = -2\Omega$.

penetration depths vanish while the other half retain a finite penetration depth set by the gap size.

*Model.*—Consider the odd Navier-Stokes equations describing a compressible time-reversal and parity violating fluid,

$$\partial_t \rho(\mathbf{r}, t) = -\rho_0 \nabla \cdot \mathbf{v}(\mathbf{r}, t) \tag{1}$$

$$\partial_t \mathbf{v} = -c^2 \nabla \rho / \rho_0 + \omega_B \mathbf{v}^* + \nu^o \nabla^2 \mathbf{v}^*, \tag{2}$$

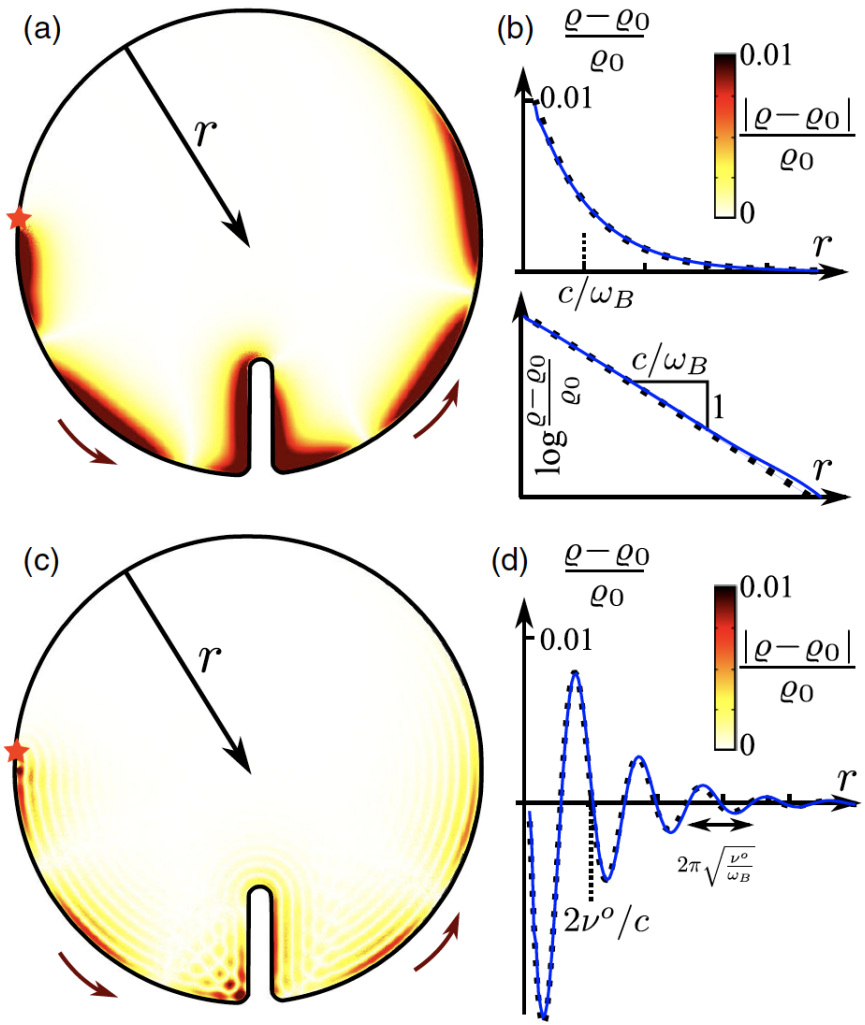


Souslov et al., PRL **122**, 128001 (2019)

# Are wall modes topologically protected?

Do topologically protected states exist in driven dissipative 3D flows? Zhang and Xie, JFM **999**, A65 (2024) show that the linearized vector eigenfunction is associated with a nonzero Chern number, computed by integrating the Berry curvature over the Brillouin zone. But

- The eigenfunctions they use do not satisfy the correct boundary conditions at the top of the layer
- It is not clear that in forced dissipative systems a nonzero Chern number is associated with topological protection

Nevertheless, the wall modes behave like they are indeed a protected state. The recent work by Vasil et al (arXiv:2409.20541.pdf) on wall modes in the limit $E \to 0$, following earlier work on bulk modes (Julien et al., GAFD **106**, 392 (2012)), applies to domains of arbitrary horizontal cross-section:

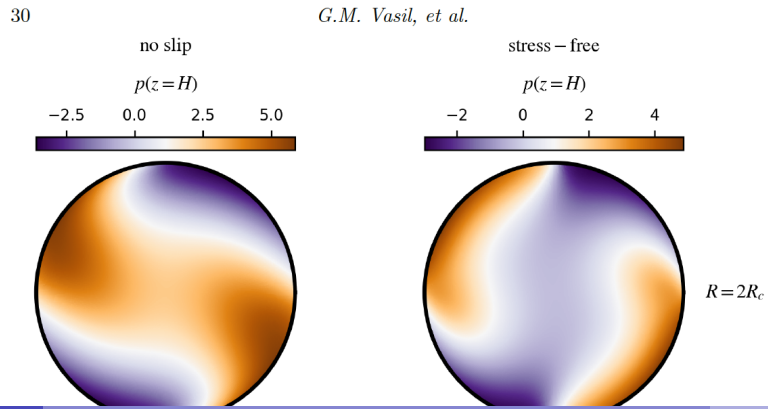

# Wall mode suppression

Wall modes are a pest when studying geostrophic turbulence in the lab. The following experimentally realizable procedure eliminates their effect:

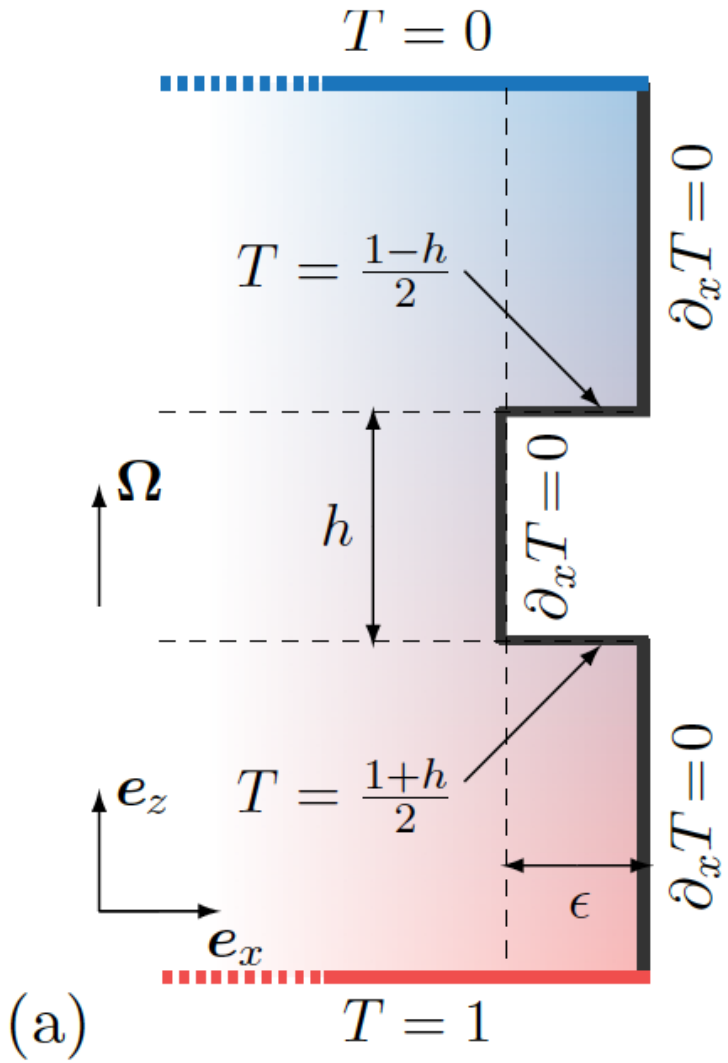


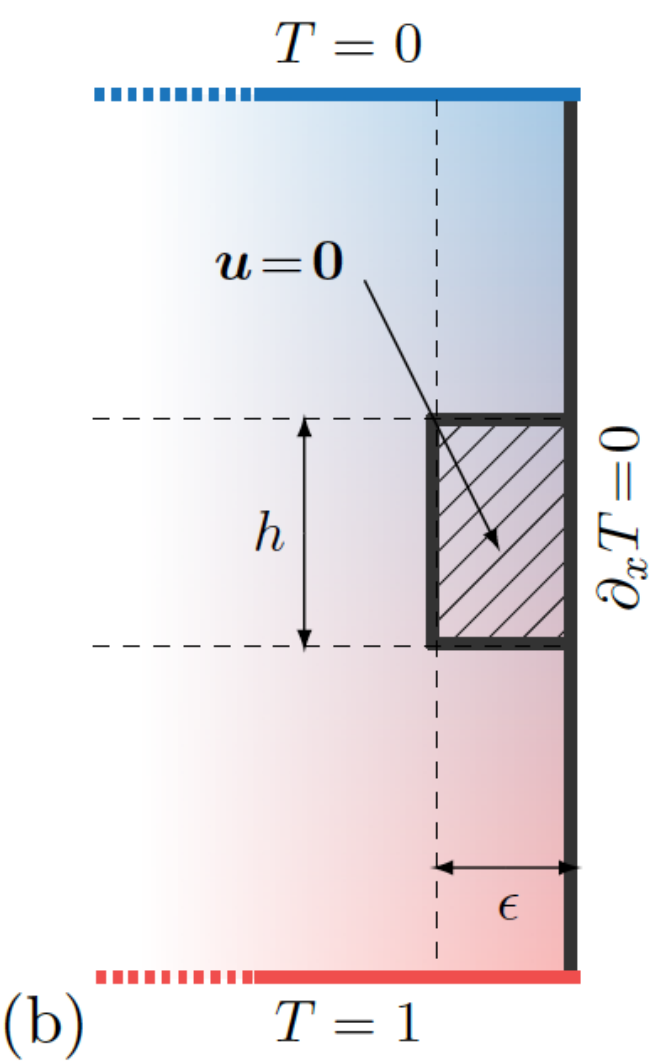

# Wall mode suppression

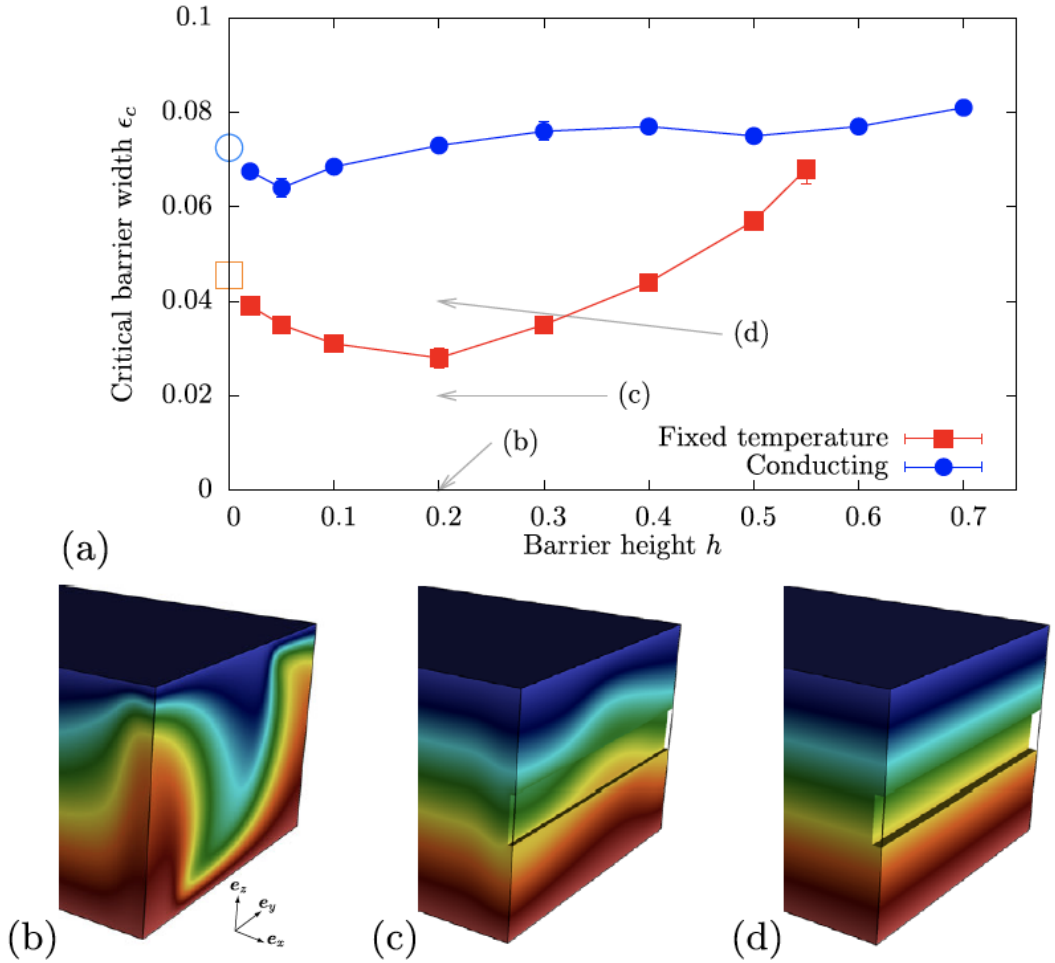


FIG. 2. (a) Critical barrier width $\epsilon_c$ as a function of its height $h$ for $E = 10^{-4}$ and $Ra = 2Ra_c^{\text{wall}} \approx 6.8 \times 10^5$. The bottom row shows side visualizations of the temperature field for (b) the case without barrier, (c) $h = 0.2$ and $\epsilon = 0.02$, and (d) $h = 0.2$ and $\epsilon = 0.04$. All three cases are indicated using arrows in (a).

# Wall mode suppression

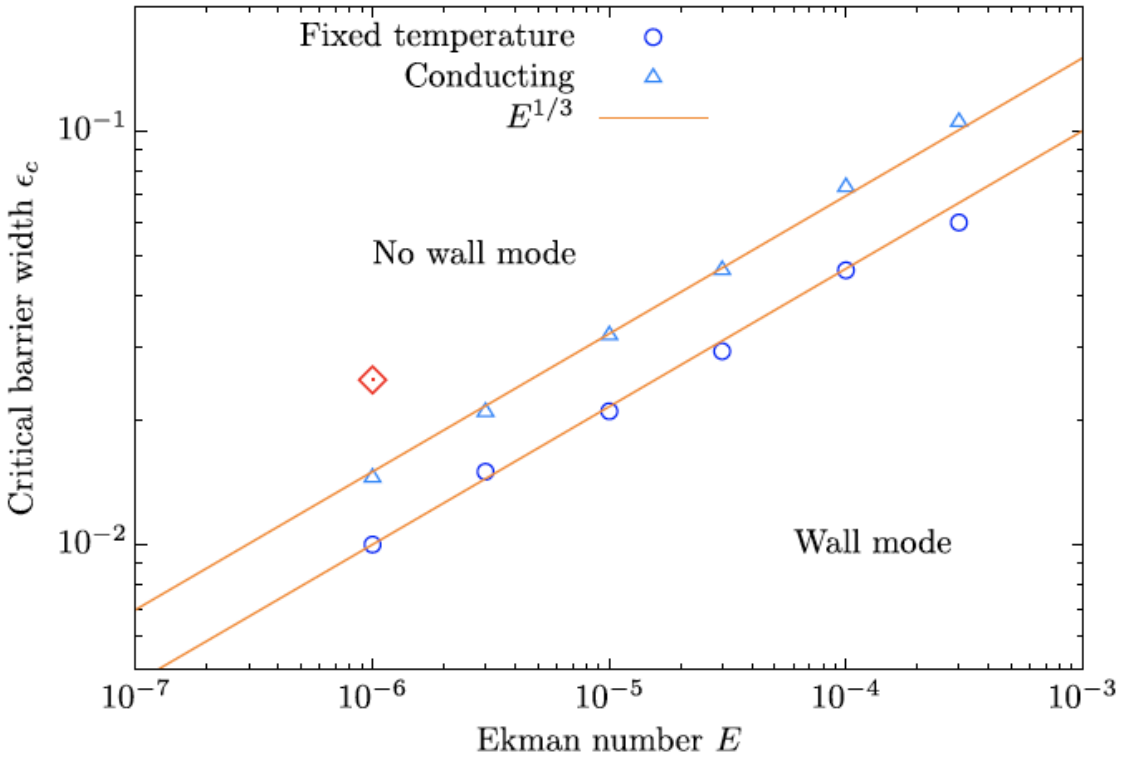


FIG. 3. Critical barrier width $\epsilon_c$ as a function of $E$ for infinitely thin fixed-temperature or conducting barriers. The Rayleigh number is fixed at twice its onset value, which itself depends on $E$. The red diamond indicates the regime considered for the experimentally relevant simulations shown in Fig. 6.

Terrien, Favier and Knobloch, PRL **130**, 174002 (2023)

# Wall mode suppression

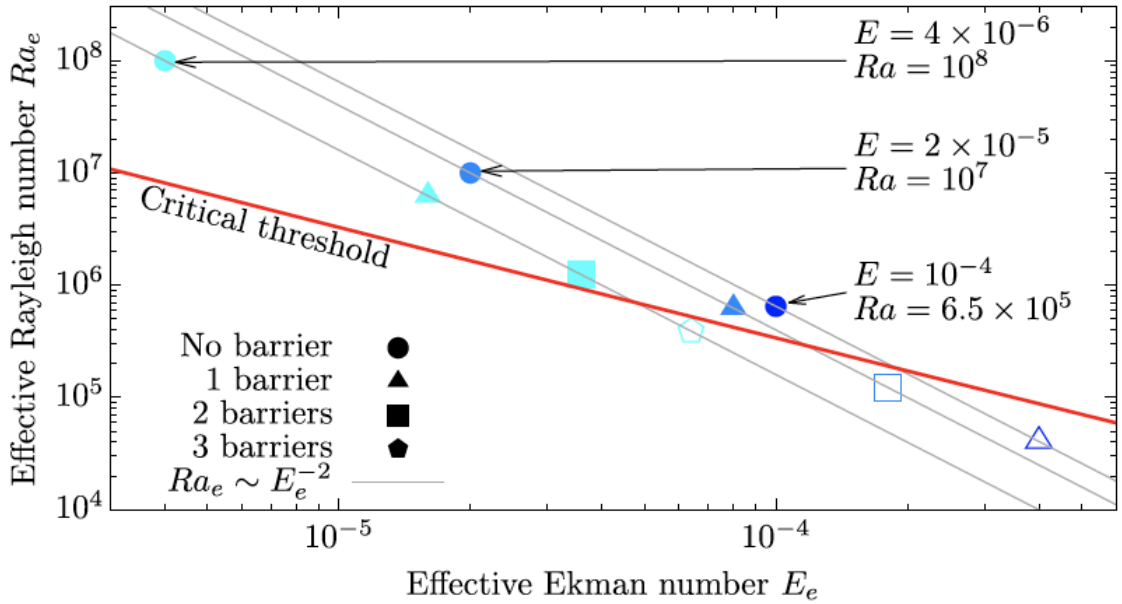


FIG. 5. Effective Rayleigh number $Ra_e$ versus the effective Ekman number $E_e$. The symbols indicate the number of barriers starting from $N = 0$ where $Ra_e = Ra$ and $E_e = E$. Filled (empty) symbols indicate growing (decaying) wall modes. The thick red line is the critical curve for the onset of wall modes predicted by linear theory [35] while the thin gray lines show the $Ra_e \sim E_e^{-2}$ scaling.

$$E_e = Ed^{-2} = E(N+1)^2, \quad Ra_e = Rad^4 = Ra(N+1)^{-4}. \quad (4)$$

# Wall mode suppression: $Ra = 3 \times 10^9$, $E = 10^{-6}$

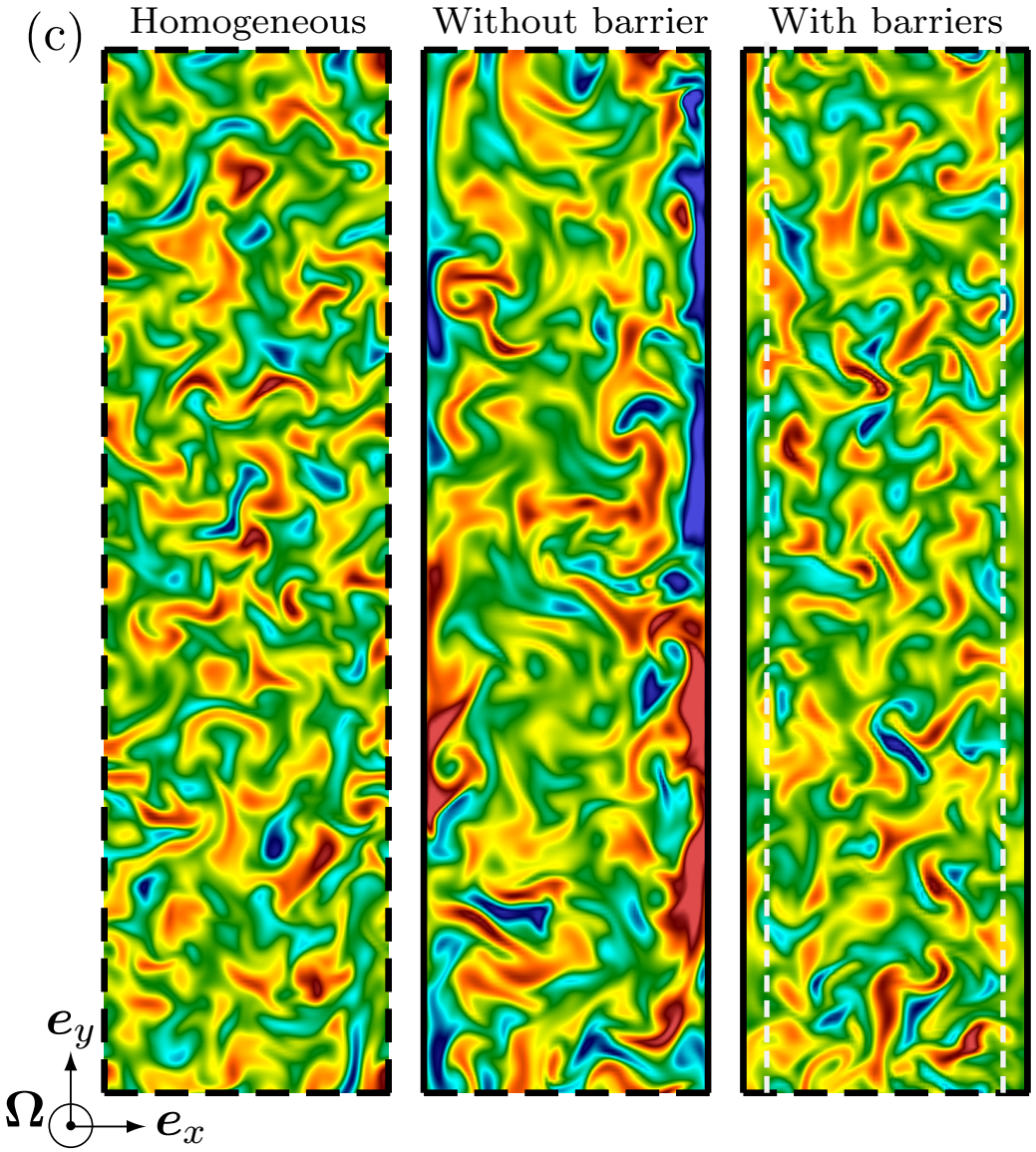


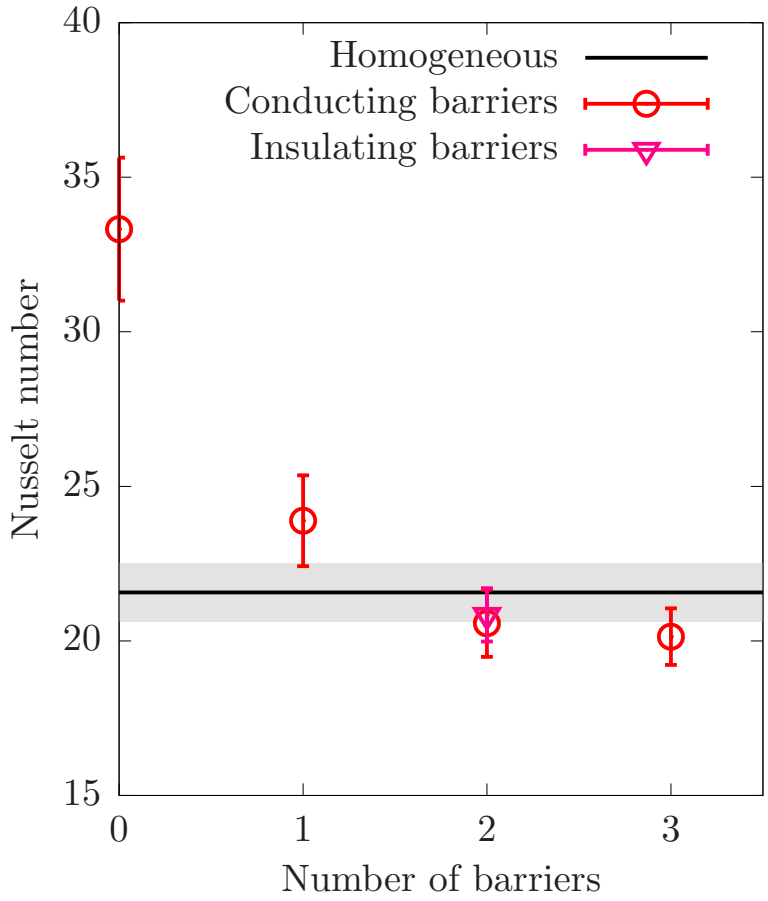


Two horizontal barriers reduce Nu to its homogeneous value (no sidewalls)

# Wall modes and the Swift-Hohenberg (SH35) equation



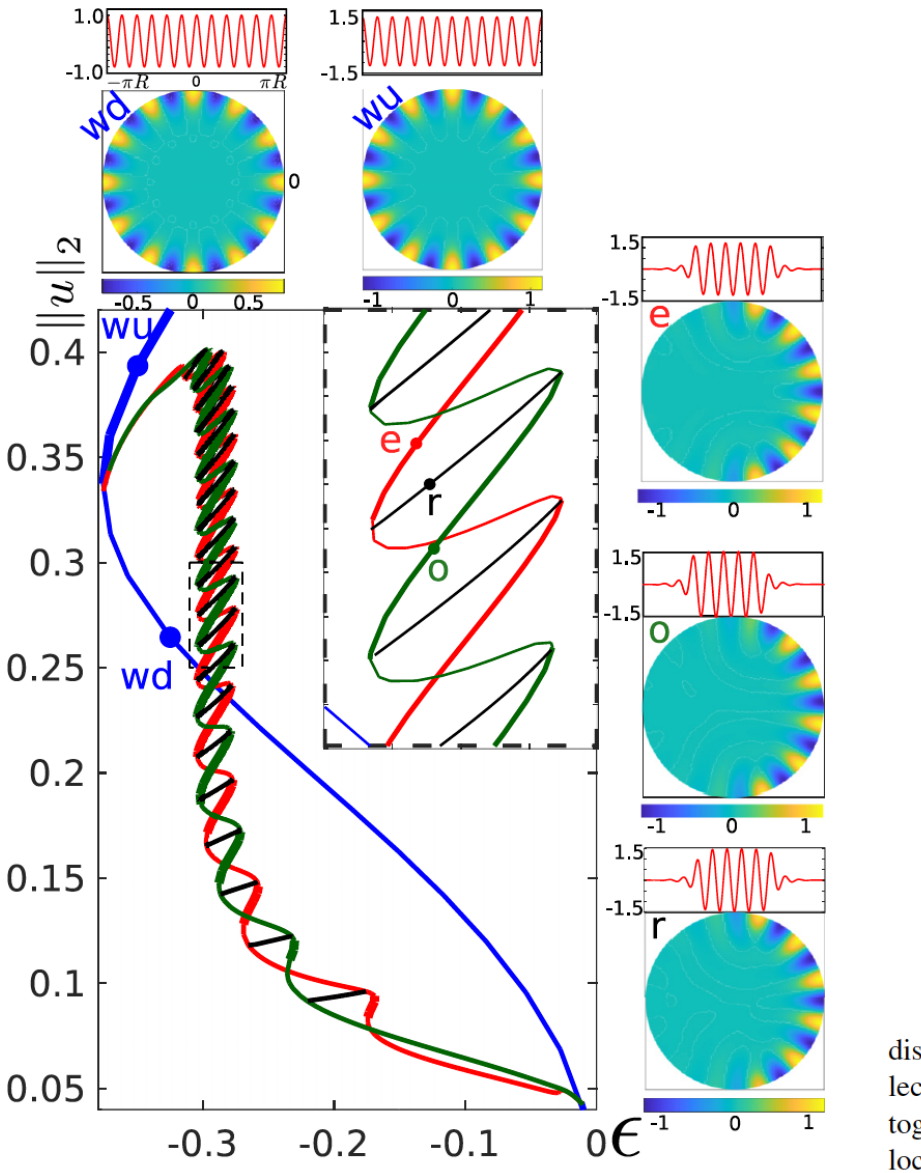


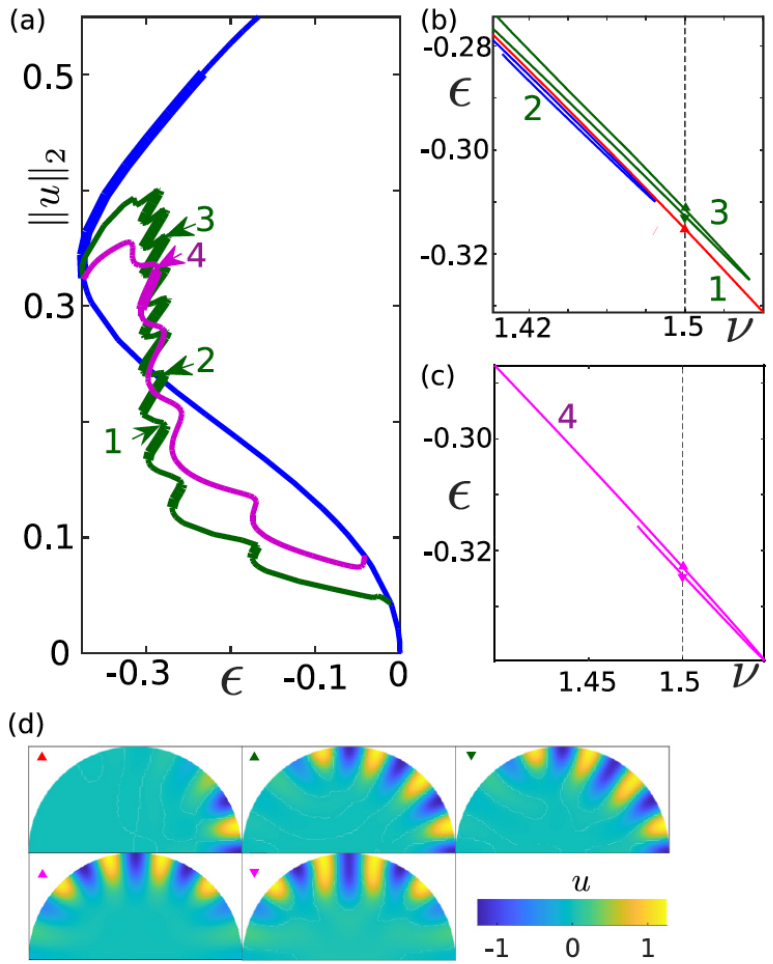


FIG. 13. Branches of one- and two-pulse solutions on the half disk for the case $R = 14$, $q = 1$, together with continuation of selected folds in $\nu$. (a) Bifurcation diagram of the daisy branch (blue), together with the branches of 1-pulse (green) and 2-pulse (magenta) localized daisy states when $\nu = 1.4$, with four representative folds

# Bulk modes and the Swift-Hohenberg (SH35) equation



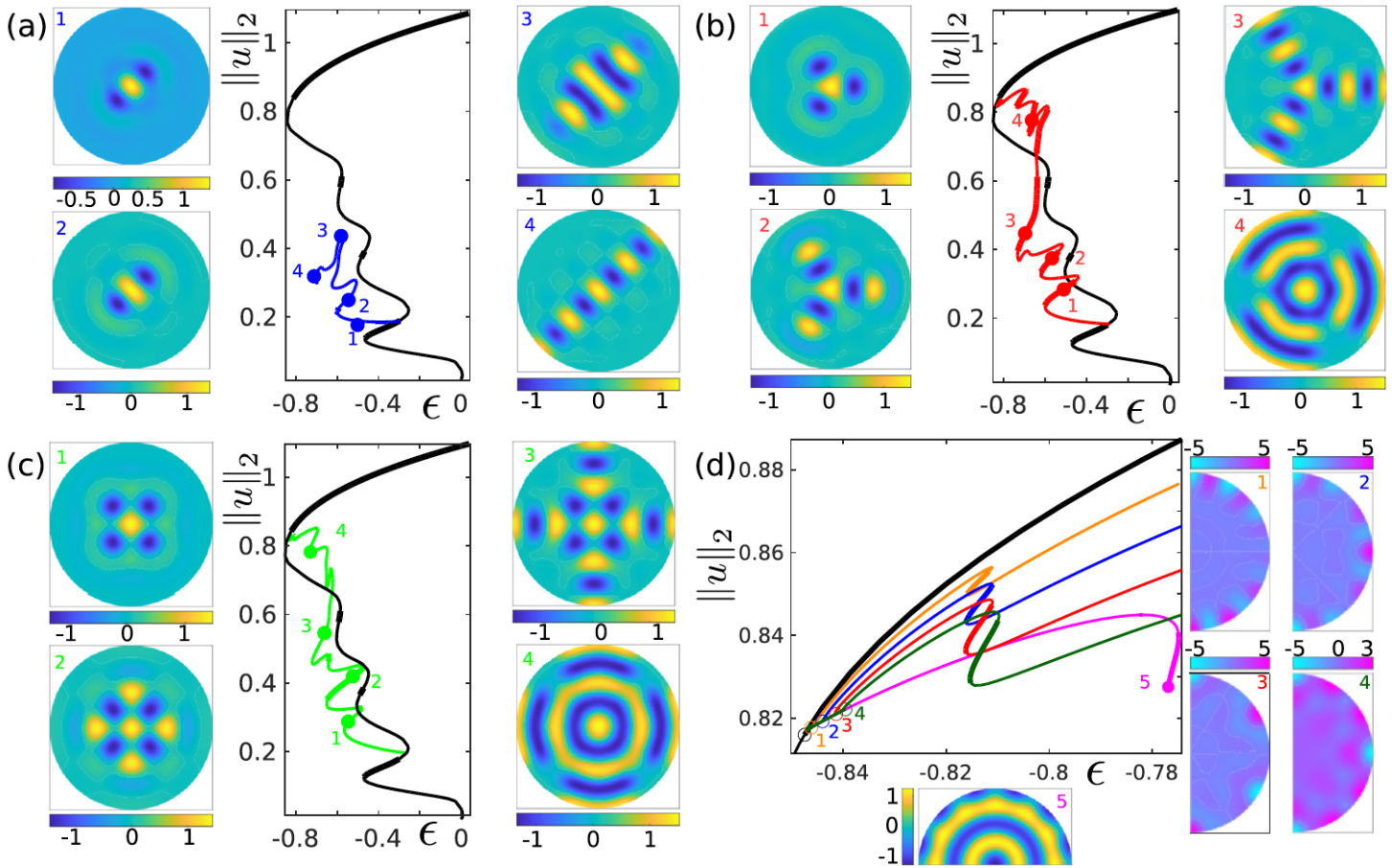


FIG. 9. Branches of multiarm solutions for $R = 14$, $\nu = 2$, $q = 1$. (a)–(c) $m = 2, 3, 4$ branches bifurcating from an axisymmetric spot at low $\|u\|_2$. Stability with respect to perturbations on the full disk is indicated by thick line segments. In each case, illustrative solutions are numbered and shown in corresponding insets. (d) Zoom of the bifurcation diagram with the $m = 12$ crown branch (magenta) and the branches of 1-arm (orange), 2-arm (blue), 3-arm (red), and 4-arm (green) states that bifurcate from it; the $m = 3, 4$-arm states connect to the corresponding branches in panels (b) and (c). The four critical eigenfunctions on the $m = 12$ crown branch are shown alongside, together with the solution profile at location 5 on this branch. See Fig. 10 for further continuation and sample profiles along the $m = 1, 2$ branches bifurcating from the first two bifurcation points on the crown branch.

# Bulk modes and the Swift-Hohenberg (SH35) equation



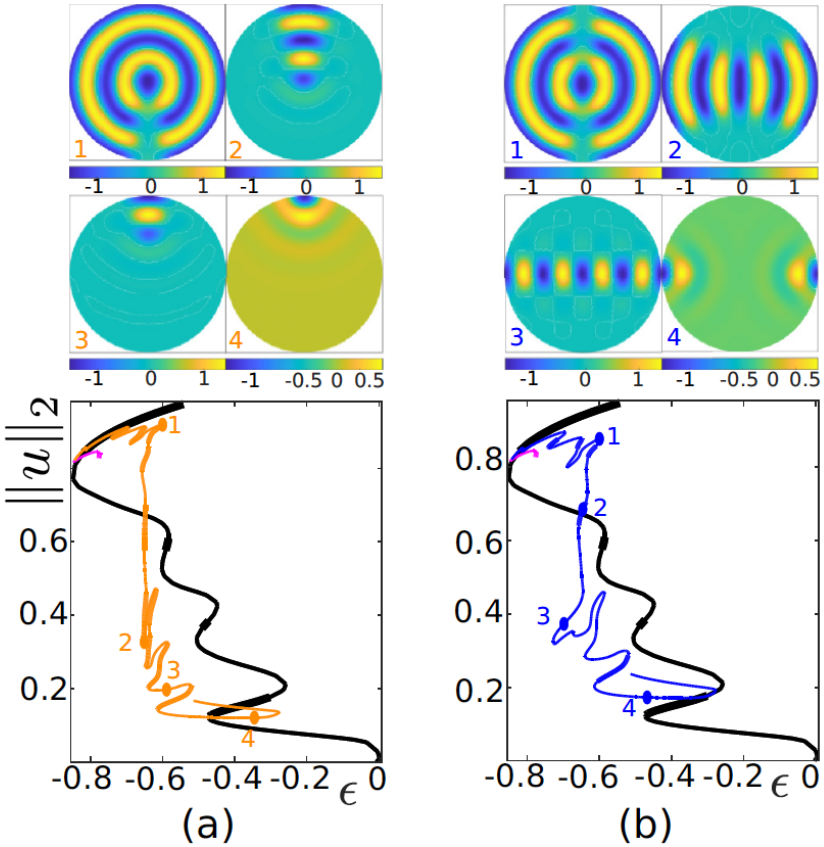


FIG. 10. Continuation of Fig. 9 showing the $m = 1, 2$ branches from their origin on the $m = 12$ crown branch. Stability with respect to perturbations on the full disk is indicated by thick line segments.

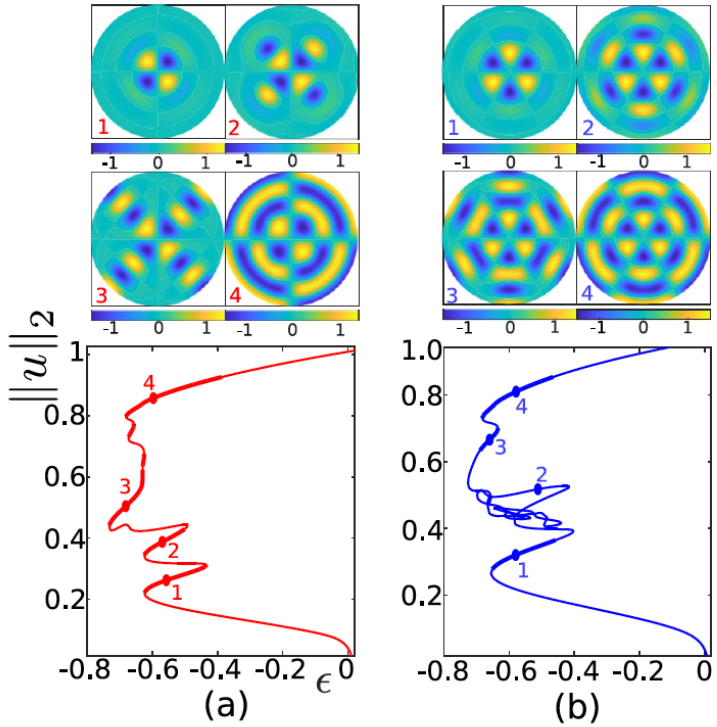


FIG. 11. Branches of solutions with the symmetry $D_m^-$ emerging from bifurcations of the trivial state $u = 0$. Panels (a) and (b) show the $4^-$-arm and $6^-$-arm states, respectively. The bottom panels show the corresponding bifurcation diagrams in red and blue. Sample states at locations indicated by filled dots are shown in the top panels. Stability with respect to perturbations on the full disk is indicated by thick line segments.

Verschueren et al., PRE **104**, 014208 (2021)

# Equatorially trapped convection: $\epsilon^2 = \ell/R$



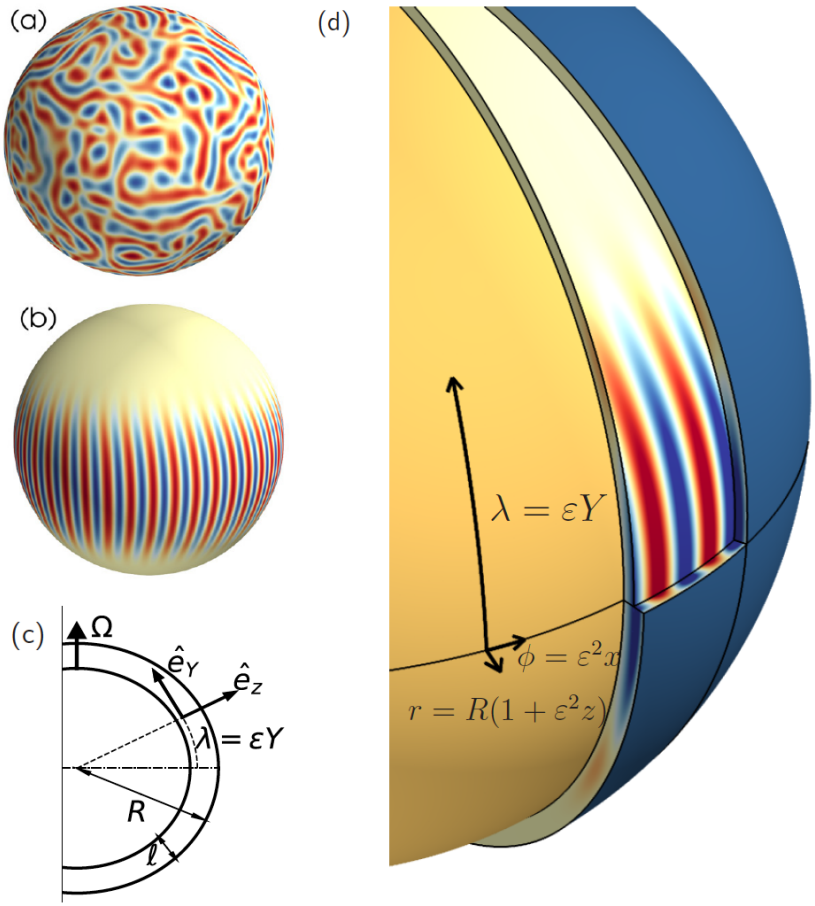


FIG. 1. Shell slices of temperature taken at mid-depth of a shallow shell with aspect ratio $\ell/R = 0.05$ in (a) slow and (b) rapid rotation. Equatorial and meridional slices of the temperature field in case (b) are represented in a three-dimensional (3D) visualization in (d). In (b) and (d) convective motions adopt the form of anisotropic Taylor columns localized in the equatorial region. The equatorial reduced coordinates $(x, Y, z)$ [see Eq. (5)] are represented from the side in (c) and in perspective in (d).

# Equatorially trapped convection: $\epsilon \sim E$, $\beta = \epsilon/E = \mathcal{O}(1)$

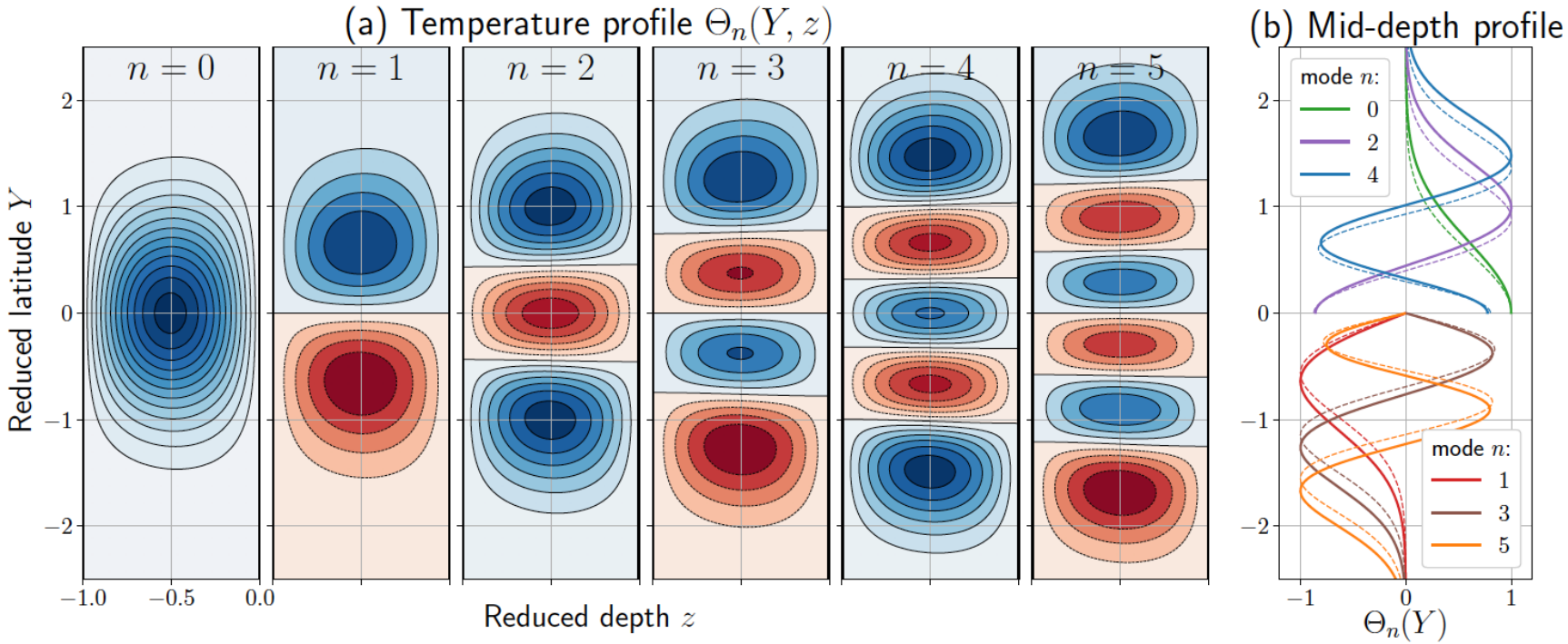


Miquel et al., PR Fluids **3**, 053801 (2018)

# Equatorially trapped convection

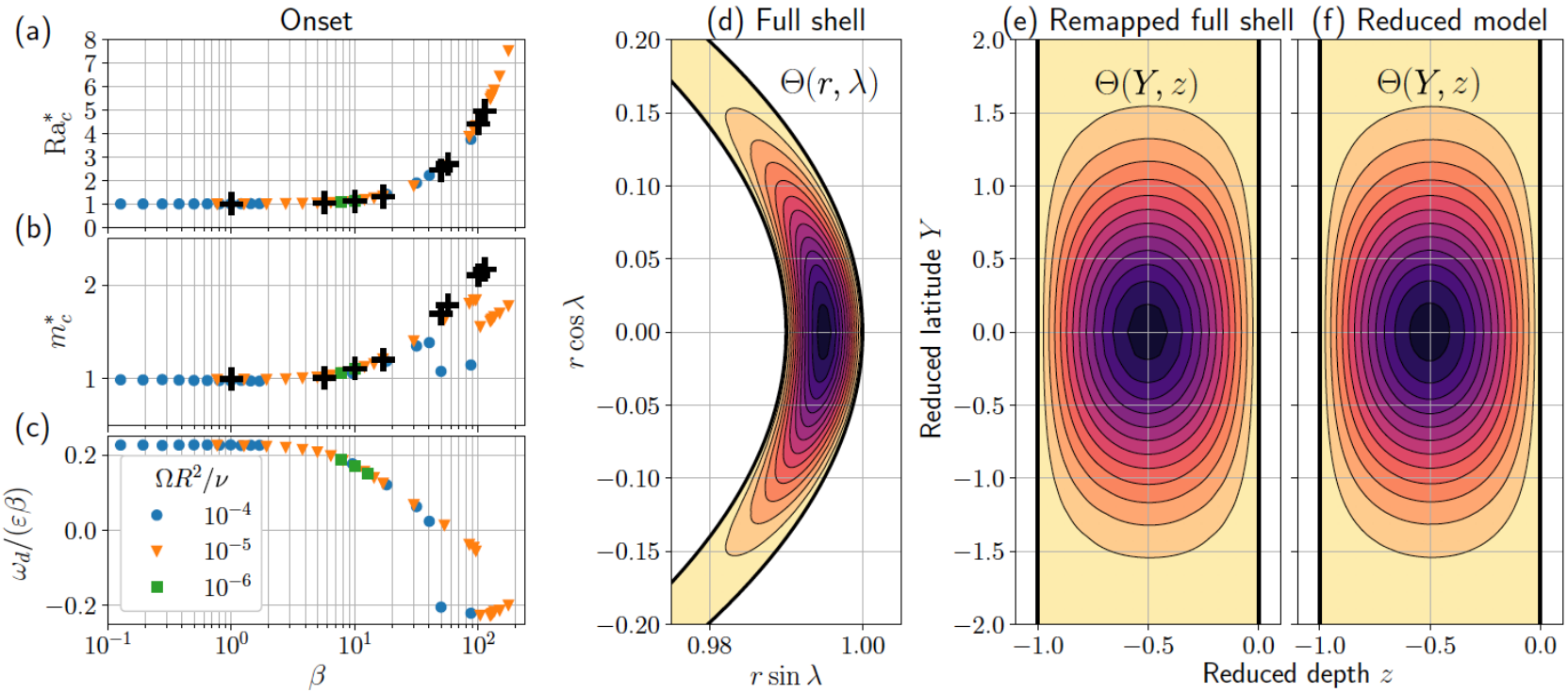


FIG. 6. (a) Normalized threshold $\mathrm{Ra}_c^*$ and (b) critical wave number $m_c^*$ for both the Boussinesq equations [Eqs. (1), color symbols] and the reduced model [Eqs. (8), black crosses] as functions of $\beta$. (c) Normalized drift frequency $\omega_d/(\varepsilon\beta)$ at onset. (d)–(f) Meridional temperature profiles of the onset mode in the Boussinesq equations and in the reduced model for the parameters $\mathrm{E} = 10^{-2}$, $\varepsilon = 0.1$ (shell), and $\beta = 10$ (reduced model). To facilitate comparison, the marginal mode of the full shell is mapped onto the reduced coordinates $(Y, z)$ in (e).

Miquel et al., PR Fluids **3**, 053801 (2018)

# Equatorially trapped convection

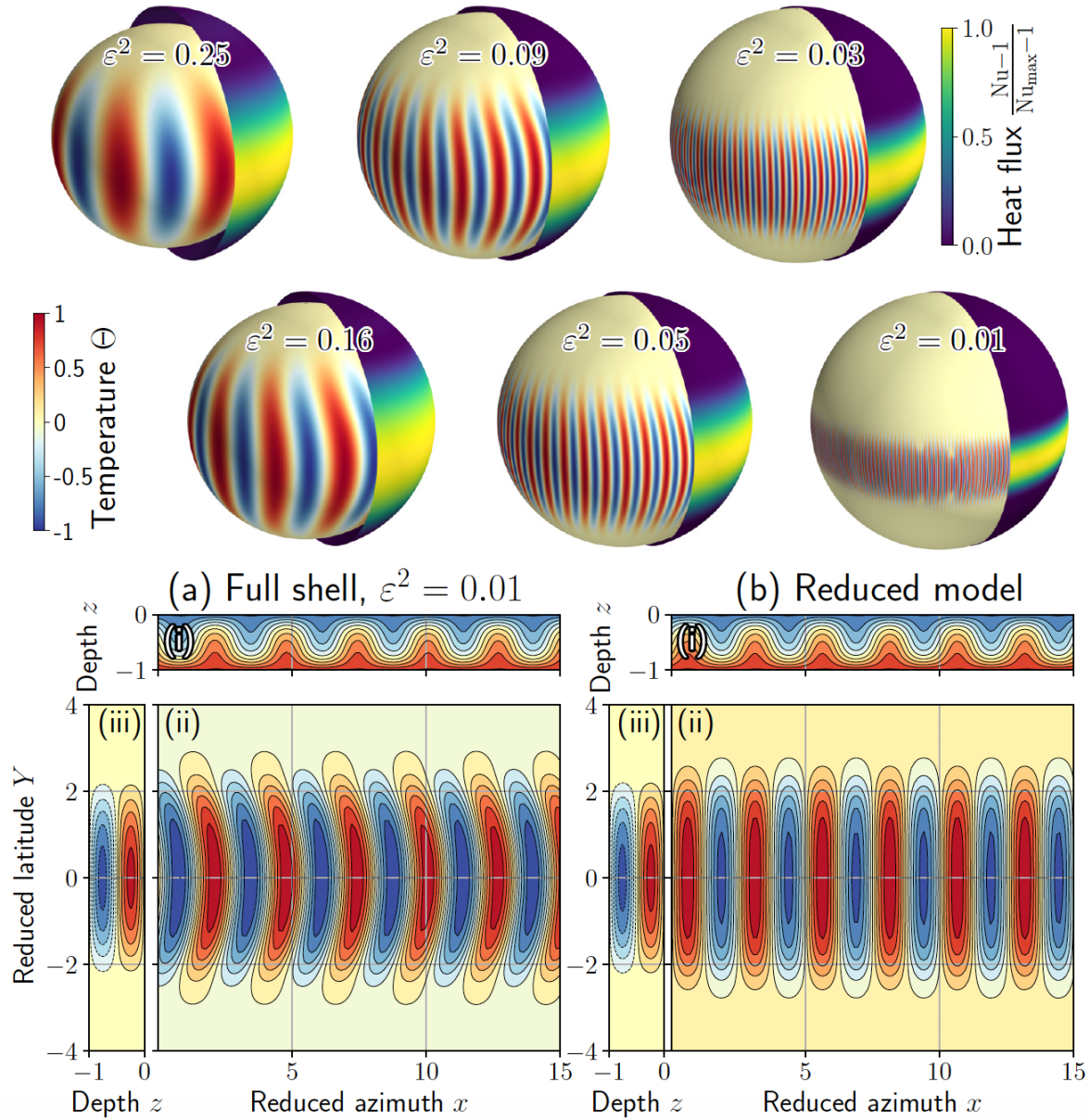

# Equatorially trapped convection

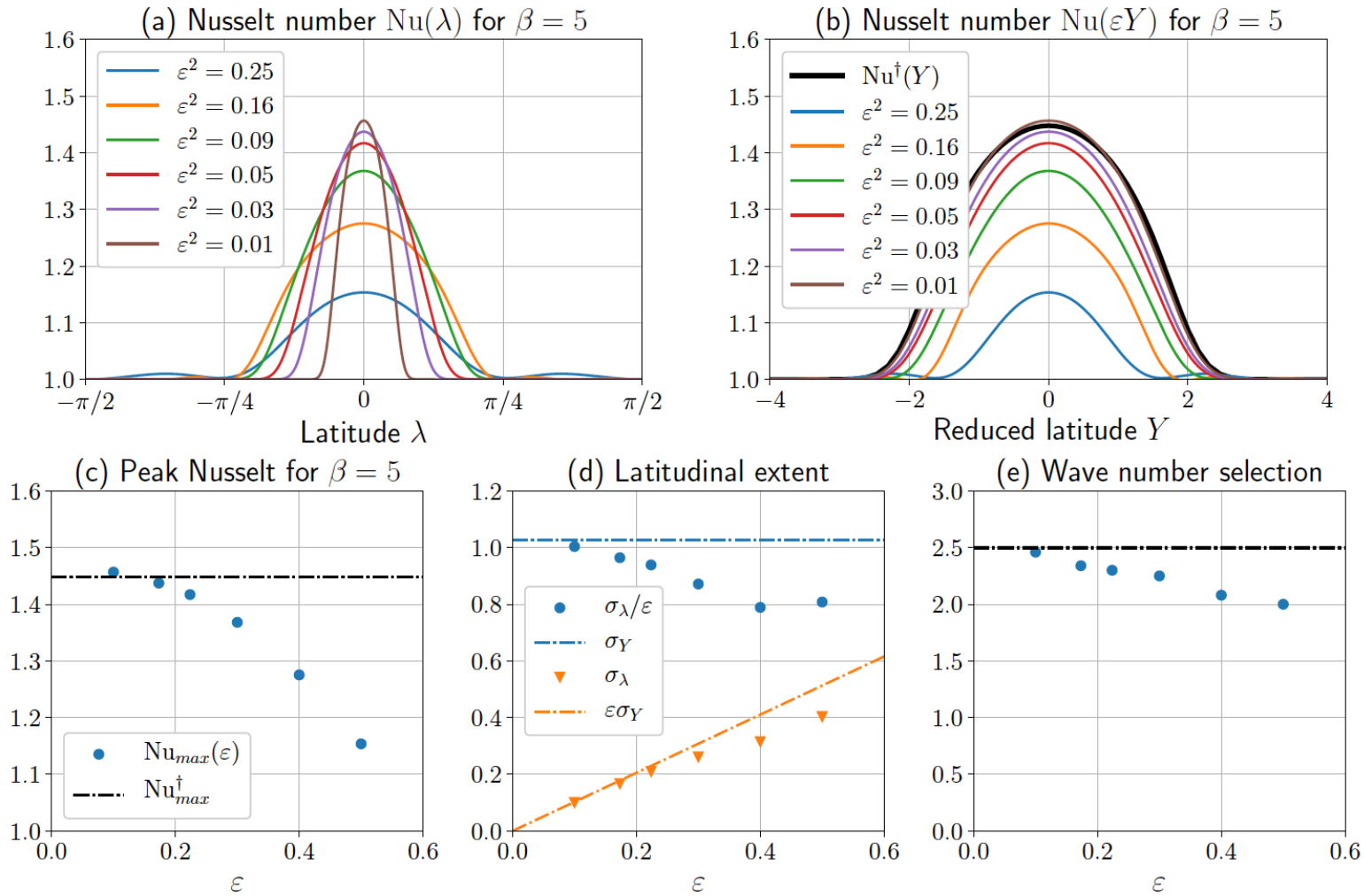


FIG. 9. Top: Heat flux Nu in the six cases plotted as a function of (a) the latitude $\lambda$ and (b) the reduced latitude $Y$, for comparison with the reduced heat flux $\mathrm{Nu}^\dagger(Y)$. Bottom: (c)–(e) $\mathrm{Nu}_{\max}$, the latitudinal extent $\sigma_Y$ or $\sigma_\lambda$ [Eqs. (18) and (20)], and the scaled wave number $M = m/\varepsilon^2$ selected after saturation, all as functions of $\varepsilon$. Dashed lines indicate the predictions from the E$\beta$C model.

# Summary

- Wall modes are a generic property of pattern-forming systems
- In 3D driven dissipative systems like RRBC they exhibit their own dynamics
- In chiral systems they appear to be robust with respect to the onset of bulk turbulence and domain geometry
- This property may be due to topological protection
- In 3D the modes may be suppressed via horizontal fins embedded in the wall, potentially enabling laboratory studies of geostrophic turbulence
- In rotating spheres the equator serves as a boundary supporting wall modes, cf. Topological origin of equatorial waves, by P. Delplace, J.B. Marston, A. Venaille, Science **358**, 1075-1077 (2017)